Physics – Uspekhi **69** (2) 169 – 188 (2026)

INSTRUMENTS AND METHODS OF INVESTIGATION PACS numbers: **07.57. – c**, 42.25.Ja, 42.81.Gs

Physical principles of filtration and the design of terahertz radiation filters

A.K. Kaveev, G.I. Kropotov

DOI: https://doi.org/10.3367/UFNe.2025.11.040059

Contents

Abstract. Present review examines the basic physical principles of operation of terahertz radiation filters. The main types of filters are presented, namely, based on absorbing/scattering materials, metamaterials (frequency-selective surfaces), interference, polarization, and some exotic types. The basic principles of calculating the filters transmission based on matrix methods are described, as well as based on solving Maxwell's equations. The areas of application of THz filters are listed.

Keywords: THz, cutoff filters, high-pass filters, band-pass filters, notch filters, absorption, metamaterials, frequency-selective surface

1. Introduction

The terahertz (THz) frequency range (100 GHz–10 THz) occupies a significant portion of the electromagnetic spectrum, lying between the microwave and infrared (IR) spectral regions. For a long time, this range has remained relatively unexplored due to technological limitations in the development of THz radiation sources and detectors. This range is attractive due its wide range of applications in secure telecommunications; spectroscopy for determining the composition of complex organic compounds, whose vibrational and rotational molecular energy levels lie in the THz range; alarm and security systems; and the detection of narcotics, explosives, and weapons [1–7]. Terahertz radiation also finds application in medicine and tomography [4, 8], as well as in the development of secure short-range wireless communication systems. The development of optoelectronic technology in the THz range over the past twenty years has further increased the demand for passive optical components designed for this frequency range.

The need to filter certain subranges of THz radiation — or radiation located outside the THz range — is driven by the development of THz spectroscopy, which requires operation in strictly defined spectral regions. For the same reason, filtering of THz radiation is essential in astronomy and astrophysics, as well as in THz sensor technologies. The most widely used technique is terahertz time-domain spectroscopy (THz-TDS), which, together with Fourier spectroscopy, serves as a primary tool for investigating the transmission properties of materials in the THz range. This technique enables determination of optical characteristics such as the complex refractive index, absorption coefficient, dielectric constant, and related parameters [9].

Known are several main types of THz filters operating on different physical principles. These include filters based on absorbing and/or scattering materials, as well as filters based on metamaterials or photonic crystals. More unconventional approaches are also considered and discussed in this review. Traditional materials used for THz filtering via absorption and scattering include nonpolar polymers such as polyethylene, polypropylene, or Teflon, combined with crystalline

A.K. Kaveev [(1,*)], **G.I. Kropotov** [(2)]
[(1)] Ioffe Institute,
ul. Politekhnicheskaya 26, 194021 St. Petersburg, Russian Federation
[(2)] Tydex LLC,
ul. Domostroitel'naya 16, 194292 St. Petersburg, Russian Federation
E-mail: [(*)] kaveev@mail.ioffe.ru

Received 16 March 2025, revised 9 November 2025
Uspekhi Fizicheskikh Nauk **196** (2) 182 – 204 (2026)
Translated by I.A. Ulitkin

materials that are transparent in the THz range, such as high-resistivity silicon or crystalline quartz. Each material possesses its own transmission band, and an appropriate combinations of these materials make it possible to achieve the desired spectral characteristics. Metamaterial-based filters are fabricated from metal foils or arrays of periodically repeating metal patterns on a THz-transparent substrate. Depending on their configuration, such filters are designed to pass a specific frequency band (bandpass filter), suppress a specific frequency band (notch filter), or cut off frequencies at either the lower or upper edge of the spectral range (cutoff filter).

This review discusses the main passive optical elements used for THz radiation filtering: cutoff filters, bandpass filters, and notch filters. Section 2 examines the fundamental physical principles of THz radiation filtering, including the general theory of radiation propagation in periodically structured media. Section 3 discusses filters based on absorbing and scattering materials. Section 4 is devoted to metamaterial-based filters. Section 5 describes polarization filters, and Section 6 describes THz plasmonic filters. Finally, Section 7 provides an overview of more exotic approaches to THz filtering.

2. Basic physical principles of THz radiation filtering

2.1 Filtration of THz radiation in absorbing layers

Most materials are opaque in the THz spectral region. The absorption of THz radiation is associated with the transfer of radiation energy to the material. Four principal mechanisms of energy loss in THz radiation during absorption can be distinguished: (1) absorption by free charge carriers, (2) absorption by lattice modes of the material (phonons) or absorption by vibrational/rotational levels of organic molecules, (3) absorption due to relaxation in polar dielectrics, and (4) disorder-induced absorption in amorphous materials. Let us briefly consider these four scenarios.

1. Free charge carriers are absorbed because the presence of free charge carriers in a material leads to a complex, frequency-dependent electrical conductivity. In turn, the complex conductivity determines the complex dielectric constant. The frequency dependence of the complex conductivity of materials is described by the Drude model [10]:

$$\sigma(\omega) = \frac{\sigma_0}{1 - \mathrm{i}\omega_0\tau_\mathrm{c}} = \frac{\sigma_0}{1 + \omega^2\tau_\mathrm{c}^2} + \mathrm{i}\,\frac{\sigma_0\omega\tau_\mathrm{c}}{1 + \omega^2\tau_\mathrm{c}^2}\,, \tag{1}$$

which yields the expression for the complex dielectric function:

$$\varepsilon = \varepsilon' + \mathrm{i}\varepsilon'' = \varepsilon_\infty + \mathrm{i}\,\frac{\sigma(\omega)}{\omega} = \varepsilon_\infty + \frac{\mathrm{i}\sigma_0}{\omega(1 - \mathrm{i}\omega\tau_\mathrm{c})}$$
$$= \left(\varepsilon_\infty - \frac{\sigma_0\tau_\mathrm{c}}{1 + \omega^2\tau_\mathrm{c}^2}\right) + \frac{\mathrm{i}\sigma_0}{\omega(1 + \omega^2\tau_\mathrm{c}^2)}\,, \tag{2}$$

where ε_∞ is the high-frequency (real) dielectric constant, σ_0 is the conductivity in a constant electric field (real), and τ_c is the relaxation time of free carriers. Figure 1a shows an example of the characteristic frequency dependence of the absorption coefficient and refractive index predicted by the Drude model. One can also see that absorption in a medium increases with increasing conductivity. Therefore, materials intended to be transparent in the THz region must have high resistance. Figure 1a also shows that free-carrier absorption is a mechanism responsible for the absorption of THz radiation, in which absorption decreases with increasing radiation frequency. Other mechanisms do not yield such a dependence.

Experimental frequency dependences of the absorption coefficient and refractive index of silicon are presented in [11] and compared with the Drude model, demonstrating good agreement. High-resistivity silicon produced by zone melting is one of the most widely used THz-transparent materials.

2. Terahertz radiation is resonantly absorbed by phonons when the frequency of the incident radiation coincides with the vibrational eigenfrequencies of the crystal lattice. Narrow

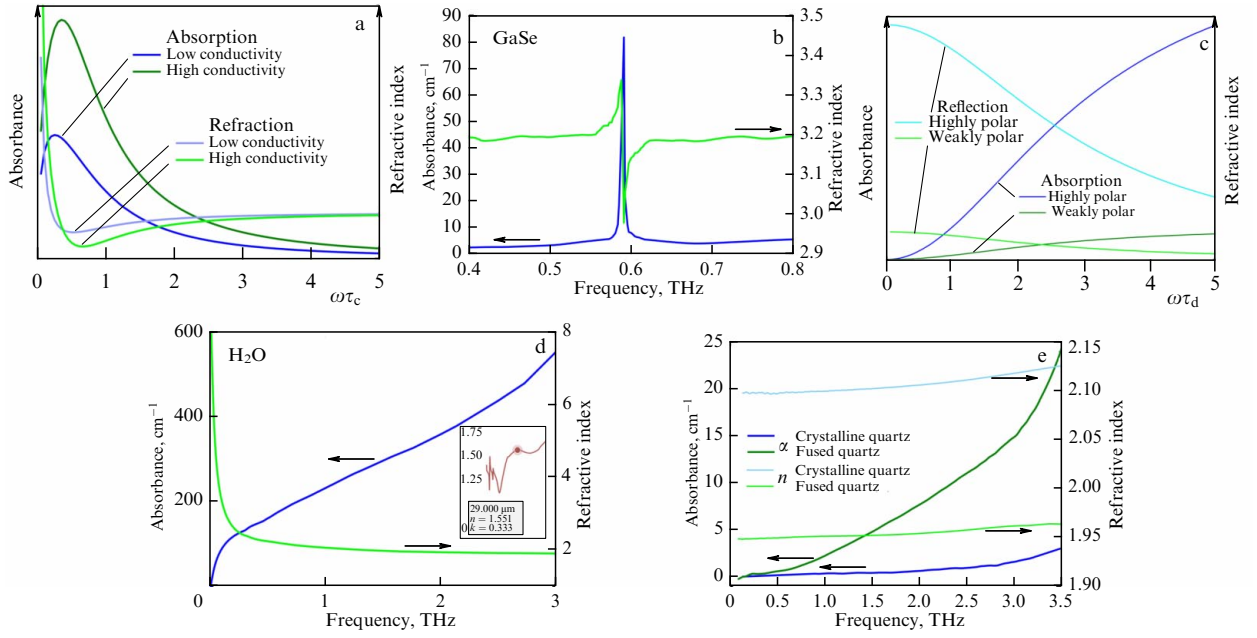

Figure 1. (a) Characteristic frequency dependence of the absorbance and refractive index predicted by the Drude model. (b) Example of this dependence for GaSe. (c) General behavior of this dependence for highly and weakly polar materials. Examples of this dependence for water (d, inset — maximum refractive index of water at the THz boundary) and (e) for crystalline and fused quartz in the THz range.

phonon absorption lines can only be observed in crystalline materials. Figure 1b shows the frequency dependence of the absorption coefficient and refractive index for GaSe [12]. One can see that at certain frequencies, the material absorption increases sharply, and the frequency dependence of the refractive index exhibits pronounced features at these frequencies.

Broader phonon absorption lines, known as Reststrahlen bands, arise from the superposition of closely spaced narrow lines and can be observed in both crystalline and amorphous materials. At frequencies within these bands, the material becomes effectively opaque. Materials transparent in the THz range should exhibit phonon absorption lines outside the THz region of interest. The presence of a Reststrahlen band indicates ionic polarizability; therefore, in materials with this band, the refractive index is almost always higher at frequencies below this band than above it. At frequencies above this band, only electronic polarizability contributes to the real part of the dielectric constant, whereas below it, both electronic and ionic polarizability make a contribution. The real part of the dielectric constant is described by the Clausius–Mossotti equation:

$$\frac{\varepsilon' - 1}{\varepsilon' + 1} = \frac{Np}{3\varepsilon_0}, \tag{3}$$

where p is the polarizability of the material, N is the number density of atoms or molecules, and ε_0 is the vacuum permittivity. Thus, in materials exhibiting a Reststrahlen band, the refractive index at THz frequencies is higher than, for example, at visible frequencies. Absorption of THz radiation due to excitation of vibrational and rotational energy levels of organic molecules has a different origin. Each material possesses unique absorption spectra in the THz range, enabling the creation of a database of characteristic spectra (fingerprints) for material identification.

3. Absorption due to relaxation in polar dielectrics occurs in materials containing polarizable chemical bonds. When an alternating electromagnetic field of THz radiation interacts with such bonds, charge separation occurs and oscillating dipoles are formed. At low frequencies, dipole oscillations do not impede the passage of THz radiation through the material, whereas at higher frequencies, dipole oscillations are hindered by intermolecular interactions. The latter leads to a delay in the response to radiation and, consequently, absorption. Therefore, THz-transparent dielectric materials should not be polar.

The frequency dependence of the dielectric function arising from the time delay of the dipole response, is determined from the Debye model [10]:

$$\varepsilon = \left(\varepsilon(\infty) + \frac{\varepsilon(0) - \varepsilon(\infty)}{1 + \omega^2\tau_\mathrm{d}^2}\right) + \mathrm{i}\left(\frac{\big(\varepsilon(0) - \varepsilon(\infty)\big)\omega\tau_\mathrm{d}}{1 + \omega^2\tau_\mathrm{d}^2}\right), \tag{4}$$

where $\varepsilon(0)$ is the dielectric constant at a constant electric field, $\varepsilon(\infty)$ is the high-frequency dielectric constant, and τ_d is the dipole response time. In polar materials, the difference $\varepsilon(0) - \varepsilon(\infty)$ is typically large. Figure 1c illustrates the frequency dependence of the absorption coefficient and refractive index for strongly and weakly polar materials, and Fig. 1d shows the behavior of these dependences for water [13].

Absorption increases with increasing values of both $\varepsilon(0) - \varepsilon(\infty)$ and τ_d. Obviously, absorption increases with increasing frequency, while the refractive index decreases.

4. Disorder-induced absorption occurs in all amorphous materials. The absorption spectra of such materials do not exhibit any sharp features, but the absorption coefficient increases with increasing frequency due to the presence of a continuum of lattice phonon modes. The frequency dependence of the absorption coefficient α is determined by the empirical expression $\alpha(\omega)n(\omega) = K\omega^\beta$, where K is a material-independent coefficient and $\beta \sim 2$. The presence of distinct spectral features is indicative of the crystallinity. Materials that are transparent in the THz range are therefore more often crystalline than amorphous. As an example, Fig. 1e shows the frequency dependence of the absorption coefficient and refractive index of crystalline and fused quartz in the 0–3.5 THz range [14]. Figure 1e also demonstrates that the absorption coefficient of fused quartz is significantly higher than that of fused quartz, while its refractive index is lower.

The four mechanisms of THz radiation absorption considered above form the basis for the design of low-pass absorbing filters in the THz region. By selecting materials with the appropriate absorption bands — or combinations of their materials — desired transmission characteristics can be achieved. In addition to absorption, THz filtering also relies on the scattering factor, which is characteristic of inhomogeneous materials, such as porous materials, powders and pellets pressed from them, materials with a rough surface, and textured materials. In particular, Teflon with various pore sizes (the Zitex series of materials [15]), as well as black polyethylene containing carbon microparticles as scattering centers, are used by Tydex LLC to manufacture a series of low-pass filters [16]. The magnitude of scattering of radiation for a given wavelength also depends on the size of the scattering centers or pores. In general, it is difficult to spectroscopically distinguish whether transmission losses in a material arise predominantly from absorption or scattering, particularly when the absorption edge lacks distinct features. An example of the analysis of the spectral behavior of porous materials in the THz range is presented in Ref. [17], where the transmission of polyethylene with embedded sucrose particles of different diameters is investigated. Franz et al. [18] also demonstrated the increasing behavior of the absorption coefficient for various powder materials in the THz range.

2.2 Filtering of THz radiation using metamaterials

Metamaterials are artificial media composed of ordered subwavelength elements. The idea of creating and developing metamaterials was first proposed in studies conducted at Bell Labs, an American industrial research and development company [19–22]. Further development of this idea, particularly for applications in IR and THz radiation filtering, was developed in papers [23, 24] devoted to lowering the plasma frequency of metal wires and generating an artificial magnetic response using metal split-ring resonators [25]. The unusual properties of metamaterials at microwave frequencies were first demonstrated in papers [26, 27], where plasmonic metal wires combined with an array of split-ring resonators exhibited simultaneously negative dielectric constant (ε) and magnetic permeability (μ). Such media were shown to possess a negative refractive index. Materials with negative ε and μ were first predicted over 40 years ago [28], but they do not occur in nature. Interest in the exotic properties of metamaterials has led to the discovery of ultra-high resolution in optical imaging, near-perfect radiation absorption, electromagnetic cloaking [29–42], and the development of transformation optics [43–53]. Potential applications of metamater-

ials also include the development of electromagnetic radiation filters, medical devices, aerospace applications, sensors and sensing systems [54–56], superprisms [57], and superlenses [58–67], including those for the THz range that enable imaging of an object beyond the diffraction limit. Comprehensive reviews of metamaterials can be found in [68–71].

Terahertz metamaterials are composite structures consisting of several elements made of metals or plastics. Owing to the ability to tailor their geometric parameters, THz metamaterials play an important role in mastering the THz range. Terahertz modulators and filters have been developed based on these structures. This section focuses on the use of metamaterials as THz radiation filters.

2.2.1 Concept of a frequency-selective surface. The concept of a frequency-selective surface (FSS) is of great importance in the creation of metamaterials. For a plane electromagnetic wave incident normally from the left onto a flat metal surface, the electric field vector **E** of the source lies in the same plane. Part of the wave energy is converted into the kinetic energy of electron oscillations in the metal. If all the wave energy is transferred to the electrons, the transmittance of such a surface will be zero. If there is a preferred direction (an infinitely thin 'wire') in the plane of the metal that is also orthogonal to the **E** vector of the incident plane wave, the electron will only move along this wire and will not acquire kinetic energy by absorbing the incident electromagnetic wave; i.e., it will be 'invisible' to it. In this case, the wave will completely pass through the metal plate. The portion of the wave energy transferred to the electron causes it to oscillate. The oscillating electron, in turn, is a dipole source of electromagnetic radiation propagating on both sides of the plane. The electron radiation emitted to the right destructively interferes with the wave transmitted through the plane, resulting in suppression of the electric field to the right of the plane. The dipole radiation emitted to the left represents a reflected wave, which determines the basic mechanism by which a plane with a preferred direction (if the reflectivity depends on the incident wavelength) functions as a THz filter: if most of the incident wave energy is re-emitted by electrons, the resulting radiation suppresses the transmitted radiation, resulting in a low transmittance of the FSS. In this case, the electrons will also re-emit to the left, resulting in a reflected wave. If only a small portion of the incident wave energy is re-emitted, this suppression does not occur, and the transmittance will be high.

In general, transmission through an FSS is a function of frequency, meaning that electrons in a metal will absorb and re-emit some wavelengths more efficiently than others. The shape of the transmission curve depends on the pattern on the metal FSS (the FSS configuration), and so calculating different pattern configurations is necessary to obtain an FSS with different transmission spectra. For example, split-ring resonator-based designs are suitable for metamaterials in the microwave [72, 73], THz [74–94], and infrared [95] ranges. However, further increases in their resonant frequency are limited by enhanced losses in the metal [96].

Figure 2 shows two examples of metal unit cell designs widely used in THz metamaterials [97]. They are periodically arranged in two dimensions (2D) on a flat surface of a dielectric substrate. The capacitive annular gap in the split resonator provides coupling of the electric field, while the magnetic field provides inductive coupling to the ring circuit as a whole. Together, they form a fundamental resonant

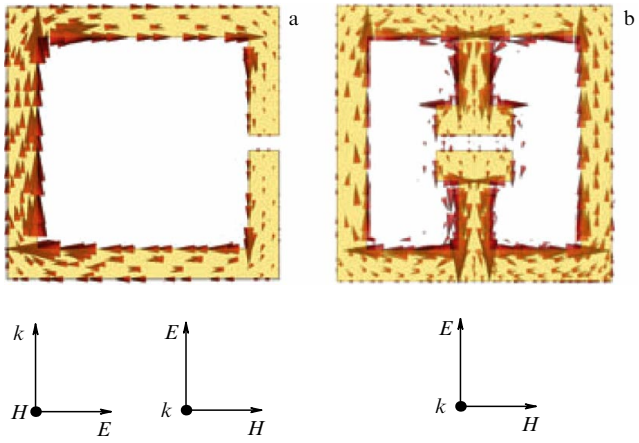

Figure 2. Examples of unit cells of THz metamaterials. (a) Single split-ring resonator. (b) Electric split-ring resonator (borrowed from [97]).

response similar to an *LC* resonator. The single split-ring resonator in Fig. 2a provides coupling to both the electric and magnetic fields of incident electromagnetic waves, while the structure in Fig. 2b enables coupling only to the electric field, resulting in a purely electric response. Azad et al. [81] described the possibility of amplifying vibrational modes depending on the geometry of the split resonator. Next, we consider THz filtering using an FSS.

2.2.2 Matrix method for calculating the FSS. A matrix formalism is used to determine the transmission and reflection properties of the FSS. A given FSS is characterized by a so-called *T*-matrix, or a cascade matrix, which depends only on the admittance of the FSS as a four-port network with characteristic complex admittance *Y*. Let us introduce the complex amplitudes of the incoming and outgoing waves on both sides of the FSS. The amplitudes of waves a_1 (incident wave) and b_1 (reflected wave) on the left side are related to the amplitudes of waves a_2 (incident wave) and b_2 (transmitted wave) on the right side through the matrix:

$$\begin{pmatrix} b_1 \\ a_1 \end{pmatrix} = \begin{pmatrix} T_{11} & T_{12} \\ T_{21} & T_{22} \end{pmatrix} \begin{pmatrix} a_2 \\ b_2 \end{pmatrix}. \tag{5}$$

Assuming that $a_2 = 0$, the ratio of the amplitudes of the reflected and incident waves is

$$r = \frac{b_1}{a_1} = \frac{T_{12}}{T_{22}}, \tag{6}$$

and the complex ratio of the amplitudes of the transmitted wave and the wave incident on the left side is

$$t = \frac{b_2}{a_1} = \frac{1}{T_{22}}. \tag{7}$$

It is important to distinguish *T*-matrix from the *S*-matrix (scattering matrix),

$$\begin{pmatrix} b_1 \\ b_2 \end{pmatrix} = \begin{pmatrix} S_{11} & S_{12} \\ S_{21} & S_{22} \end{pmatrix} \begin{pmatrix} a_1 \\ a_2 \end{pmatrix},$$

where b_1 and b_2 are the amplitudes of the waves reflected from the left and right, and a_1 and a_2 are the amplitudes of the

waves incident from the left and right. In this case, the reflectances and transmittances are given by the formulas $r = b_1/a_1 = S_{11}$, and $t = b_2/a_1 = S_{21}$ (at $a_2 = 0$). The S-matrix describes a multiport device through the amplitudes of the incident (incoming) and reflected (outgoing) waves at its ports. However, this matrix is inconvenient for analyzing cascaded four-port networks. Therefore, it is more convenient to introduce T-matrices, which, unlike S-matrices, are multiplicative when analyzing cascaded four-port networks (in our case, metal meshes).

To calculate the reflectance (R) and transmittance (T), it is necessary to calculate the squared absolute value of expressions (6) and (7). This requires determining the corresponding matrix elements T_{ij} by introducing the equivalent-circuit admittance Y. For a free-standing metal mesh, the resulting matrix has the form [98]:

$$T = \begin{pmatrix} -\dfrac{Y(f)}{2} + 1 & -\dfrac{Y(f)}{2} \\ \dfrac{Y(f)}{2} & \dfrac{Y(f)}{2} + 1 \end{pmatrix}. \tag{8}$$

Since the admittance Y depends on the frequency $f = \omega/2\pi$, both transmission and reflection will also be functions of frequency. The formula for the admittance of a given FSS can be determined empirically. In this way, single-element free-standing FSS structures (e.g., filters) are calculated at a normal angle of incidence. It is also necessary to analyze multi-element filters, filters lying on substrates, and filters at nonorthogonal incidence of radiation. Each of these generalizations requires modifications to the formulas given above and is described in detail in [99, 100]. In particular, for a multicomponent FSS system, we introduce the inverse matrices T_i as T_i'. If a sequence of elements $M_1, M_2, M_3, \ldots$ is described by matrices $T_1', T_2', T_3', \ldots$, then we can find the matrix corresponding to the multi-element system by multiplying their individual matrices: $T'_{\text{total}} = \ldots T_3' T_2' T_1'$. The matrix T_1 is the last element in the above formula, since it corresponds to the first element on which the wave is incident. Let us define a transmission matrix that describes the change in the phase of a wave as it propagates between individual FSSs, taking into account the refractive index:

$$T_n = \begin{pmatrix} \mathrm{e}^{-2\pi \mathrm{i} f dn/c}\, \mathrm{e}^{-\alpha d} & 0 \\ 0 & \mathrm{e}^{2\pi \mathrm{i} f dn/c}\, \mathrm{e}^{-\alpha d} \end{pmatrix}, \tag{9}$$

where d is the distance between successive FSSs. The factor $\mathrm{e}^{-\alpha d}$ takes into account losses in the medium, with α being the absorption coefficient (inverse length). The matrix corresponding to a complete system consisting of several FSSs separated by distances d is

$$T'_{\text{total}} = \ldots T_3' T_{32} T_2' T_{21} T_1'. \tag{10}$$

The transmittance and reflectance of the system are obtained using formulas (6) and (7), where T_{ij} denote now the elements of the complete scattering matrix T_{total}.

The above formulas are applicable only to free-standing FSSs, such as metal meshes. In reality, meshes are often formed on substrates, and so it is necessary to describe the type of matrix for a metal mesh at the boundary of two media with refractive indices n_1 and n_2. In this case, the matrix of an individual FSS (in particular, one acting as a filter) has the form

$$T_{n_1 n_2} = \frac{1}{2n_1} \begin{pmatrix} -Y + (n_1 + n_2) & -Y + (n_1 - n_2) \\ Y + (n_1 - n_2) & Y + (n_1 + n_2) \end{pmatrix}. \tag{11}$$

This result was derived from transmission line theory [99, 100] under the assumption that the FSS element is located at the junction of two transmission lines with characteristic admittances $Y_1 = n_1$ and $Y_2 = n_2$. In general, for an FSS located between two media with refractive indices n_1 and n_2, the following relation holds for increasing the resonant wavelength: $\lambda_{\text{res}} \to \lambda_{\text{res}}[(n_1^2 + n_2^2)/2]^{1/2}$, which obviously reduces to the original form at $n_1 = n_2 = 1$. That is, the resonant wavelength of radiation entering the system from vacuum increases. Since the formula for the admittance of filters, such as cross-mesh filters, contains terms that are functions of λ_{res}, the formulas for admittance should be modified accordingly.

If the wave is normally incident on an FSS, the polarization vector will always lie in the FSS plane. If the wave is incident with a deviation from the normal, the electric field vector may or may not be in the plane of the FSS, depending on polarization of the incident wave. Thus, two orthogonal polarization states are distinguished: in-plane (p-polarization) and out-of-plane (s-polarization) of the FSS. The polarization vector for p-polarization is in the plane of the FSS, while the polarization vector for s-polarization has normal and tangential components. The normal component of the electric field cannot induce surface currents because electrons are restricted to motion in only two dimensions. This means that the normal field component will not be able to transfer energy to the electrons and will therefore completely pass through the FSS. Therefore, the reflectance and transmittance of the s- and p-polarizations will be different and must be tracked separately. If a wave is incident on the FSS at some angle ϑ, then the following will hold for the admittances of the s- and p-polarizations:

$$Y_{\text{S}} = Y \cos\vartheta\,, \quad Y_{\text{P}} = \frac{Y}{\cos\vartheta}\,. \tag{12}$$

These two relations are derived by decomposing the incident wave into waveguide modes and applying waveguide theory to determine the effective conductivity [99–101]. Next, we expand the 2×2 matrix to a 4×4 matrix composed of four 2×2 submatrices. The diagonal submatrices represent the matrices for the two polarizations, while the off-diagonal submatrices are zero:

$$T_{n_1 n_2} = \frac{1}{2n_1} \times \begin{pmatrix} -Y_{\text{S}} + (n_1 + n_2) & -Y_{\text{S}} + (n_1 - n_2) & 0 & 0 \\ Y_{\text{S}} + (n_1 - n_2) & Y_{\text{S}} + (n_1 + n_2) & 0 & 0 \\ 0 & 0 & -Y_{\text{P}} + (n_1 + n_2) & -Y_{\text{P}} + (n_1 - n_2) \\ 0 & 0 & Y_{\text{P}} + (n_1 - n_2) & Y_{\text{P}} + (n_1 + n_2) \end{pmatrix}, \tag{13}$$

where Y_{S} and Y_{P} are defined by formulas (12). The transmittance for the s-polarization is determined by the reciprocal of element (2,2), while the transmittance for the p-polarization is determined by the reciprocal of element (4,4). The total transmittance will be a linear combination of the coefficients corresponding to the two polarization states:

$$T_{\text{total}} = (\sin\vartheta_{\text{p}})^2 T_S + (\cos\vartheta_{\text{p}})^2 T_P\,, \tag{14}$$

where ϑ_p is the polarization angle, i.e., the angle between the electric field of the electromagnetic wave and the direction in the plane perpendicular to the vector k.

Specific equivalent circuits for practical FSSs are discussed in Section 4.1. The theory of FSSs is presented in more detail, for example, in [98, 101]. The theory of calculating the FSS using matrix methods is presented in detail in books [99, 100] and paper [102].

2.2.3 Fundamental theory of spatially periodic structures. This section presents a generalized approach to calculating the transmission of spatially periodic structures. There are two types of problems involving spatially periodic structures: (i) scattering problems and (ii) eigenvalue problems (or dispersion problems). In the first case, the scattered field generated by the interaction of an incident plane wave with a singly or doubly periodic open structure is investigated. In the second case (in the absence of electromagnetic wave sources), the dispersion curves of the periodic structure are studied [i.e., graphs of the Floquet constant(s) as a function of frequency]. Assuming that the periodic structure has an infinite number of periods, the Floquet theorem is applied: for a given propagation regime at a given constant frequency, the electric and magnetic fields in one cross section differ from the fields at a distance of a period only by a complex constant. When considering a single periodic structure, it is assumed that it is infinite and homogeneous in the y direction, i.e., two-dimensional. It follows from the Floquet theorem that the field $\mathbf{F}$ (i.e., $\mathbf{E}$ or $\mathbf{H}$) satisfies the equation:

$$\mathbf{F}(x, y, z + D_z) = \mathbf{F}(x, y, z) \exp(-\gamma_z D_z), \tag{15}$$

where γ_z is the Floquet constant, and D_z is the period of the structure in the z direction. Consequently, the field in a periodic structure can be written as

$$\mathbf{F}(x, y, z) = \mathbf{F}_p(x, y, z) \exp(-\gamma_z z), \tag{16}$$

where $\mathbf{F}_p$ denotes the periodic part of the field. Since $\mathbf{F}_p$ can be represented as a Fourier series, $\mathbf{F}$ is written in the form

$$\mathbf{F}(x, y, z) = \sum_{n=-\infty}^{\infty} \mathbf{G}_n(x, y) \exp\left[-\left(\gamma_z + \frac{2\pi n i}{D_z}\right) z\right]. \tag{17}$$

Each term in series (17) is referred to a spatial harmonic. In scattering problems, if the incident plane wave is neither attenuated nor amplified in the direction of the periodicity (i.e., there are no losses or gains in region 1 in Fig. 3), the complex relation $\gamma_z = i\beta_z$ holds, where β_z is a real variable. Consequently, each harmonic has a wave vector component in the direction of the periodicity, given by $\beta_{zn} = \beta_z + 2\pi n/D_z$. Furthermore, in the direction of periodicity, the Floquet constant is equal to the component of the wave vector of the incident plane wave. We demonstrate this by considering a two-dimensional singly periodic structure (see Fig. 3). The incident plane wave is assumed to have the form

$$F^{inc} = A^{inc} \exp(ik_x^{inc} x) \exp(-ik_z^{inc} z). \tag{18}$$

The plane wave is a periodic function along the z direction, and when it interacts with a periodic structure of period D_z, it generates a scattered field F_{sc}, which is also periodic with period D_z. The scattered field in regions 1 and 3 in Fig. 3 is represented by a superposition of propagating and evanescent

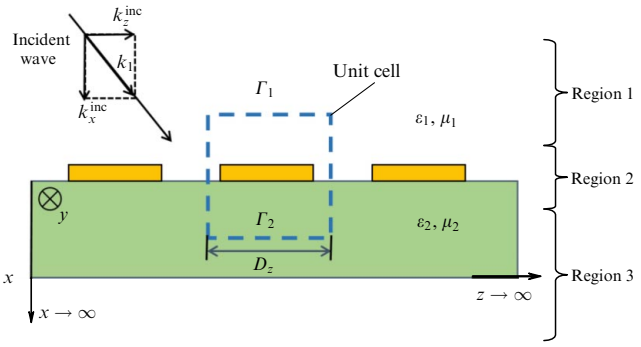

Figure 3. Open two-dimensional singly periodic structure. The unit cell is shown by a dashed line. The structure is infinite and homogeneous along the y direction. The unit cell of the structure is bounded along the x direction by two horizontal boundaries.

spatial harmonics, which are plane waves for two-dimensional singly periodic structures and TE/TM waves for three-dimensional doubly periodic structures.

Thus, the total field in regions 1 and 3 in Fig. 3, in region 1 is

$$\begin{aligned} F^{up} &= F^{inc} + F_p^{sc} \exp(-ik_z^{up} z) \\ &= A^{inc} \exp(ik_x^{inc} x) \exp(-ik_z^{inc} z) \\ &+ \sum_{n=-\infty}^{\infty} R_n \exp(-ik_x n_x) \exp\left(-i \frac{2\pi n}{D_x} z\right) \exp(-ik_z^{up} z), \end{aligned} \tag{19}$$

and in region 3 is

$$\begin{aligned} F^{low} &= F_p^{sc} \exp(-ik_z^{low} z) \\ &= \sum_{n=-\infty}^{\infty} T_m \exp(ik_x m_x) \exp\left(-i \frac{2\pi m}{D_z} z\right) \exp(-ik_z^{low} z), \end{aligned} \tag{20}$$

where $\exp(-ik_z^{up} z)$ and $\exp(-ik_z^{low} z)$ are the complex phase Floquet factors in the upper (i.e., region 1) and lower (i.e., region 3) regions, respectively. In region 2, the field is expressed as $F = F_p(x, z) \exp(-\gamma_z z)$. The continuity of the tangential field at the interface Γ_1 (at $x = x_{12}$) yields the expression

$$\begin{aligned} &\left[A^{inc} \exp(ik_x^{inc} x_{12})\right] \exp(-ik_z^{inc} z) \\ &+ \left[\sum_{n=-\infty}^{\infty} R_n \exp(-ik_{xn} x_{12}) \exp\left(-i \frac{2\pi n}{D_z} z\right)\right] \exp(-ik_z^{up} z) \\ &= \left[F_p(x_{12}, z)\right] \exp(-\gamma_z z). \end{aligned} \tag{21}$$

At points separated by a period, the periodic terms inside the square brackets are constant and, therefore, independent of z. There are an infinite number of such points, and, therefore, the only condition satisfying equation (21) for each such point is:

$$\gamma = ik_z^{inc} = ik_z^{up}. \tag{22}$$

Similarly, for Γ_2 we have

$$\begin{aligned} &\left[\sum_{m=-\infty}^{\infty} T_m \exp(ik_{xm} x_{12}) \exp\left(-i \frac{2\pi m}{D_z} z\right)\right] \exp(-ik_z^{low} z) \\ &= \left[F_p(x_{12}, z)\right] \exp(-\gamma z). \end{aligned} \tag{23}$$

Again, at points spaced by a period, the periodic terms inside the square brackets are constant and, therefore, independent of z. Then, using equation (22), we obtain

$$ik_z^{\text{low}} = \gamma = ik_z^{\text{inc}}. \tag{24}$$

Since harmonics are solutions of Maxwell's equations and, therefore, solutions of the wave equation, they must satisfy the dispersion relation, i.e.,

$$k_{xn} = \begin{cases} \sqrt{k_0^2\mu_r\varepsilon_r - k_{zn}^2}, & k_0^2\mu_r\varepsilon_r \geqslant k_{zn}^2, \\ -i\sqrt{k_{zn}^2 - k_0^2\mu_r\varepsilon_r}, & k_0^2\mu_r\varepsilon_r < k_{zn}^2, \end{cases} \tag{25}$$

where $k_0 = \omega/c$, the index r takes the values 1 or 2 for the reflected or transmitted wave, and k_{zn} satisfies the expression

$$k_{zn} = k_z^{\text{inc}} + \frac{2\pi n}{D_z}. \tag{26}$$

Thus, we can conclude that: (1) when a plane wave is incident on a periodic structure, scattering produces of an infinite sum of plane waves (transmission and reflection), called harmonics; and (2) these harmonics are either propagating or decaying, depending on which inequality from (25) is satisfied. The latter depends on the frequency, dielectric constant and magnetic permeability of the homogeneous medium in which the harmonic propagates, and the period of the periodic structure. The above analysis can be generalized to doubly periodic FSS structures in three dimensions. A more rigorous treatment of the theory of spatially periodic surfaces and FSS, including for doubly periodic structures, can be found, for example, in review [103].

3. THz filters based on absorbing materials

3.1 Spectral studies of materials for fabricating THz cutoff filters

A brief, but not exhaustive, overview of the main transmission materials for THz optics is presented below [104]. High-resistivity float-zone silicon (HRFZ-Si) with $\rho = 10$ Ω cm or higher and 25 kΩ cm or higher for n-type and p-type doping, respectively, is used for fabricating THz optics elements. It provides 50–54% transmission in the wavelength range from 50 to 8000 μm. Figure 4a shows the transmittance and reflectance spectra of HRFZ-Si in the THz range.

Another widely used material for THz optics for wavelengths above 50 μm is crystalline quartz. Figure 4b shows the transmittance spectra of 1 mm thick crystalline quartz. Crystalline quartz is a birefringent material and this property should be taken into account when radiation polarization is important.

X-cut materials are used to produce $\lambda/2$ and $\lambda/4$ wave plates operating in the THz range. Along with crystalline quartz, cheaper fused quartz can be used in THz optics, particularly, when radiation polarization is not critical. Due to the absence of long-range order, the transmittance of fused quartz is lower and significantly depends on the element thickness. Figure 4c shows the transmittance spectra of KU1 fused quartz plates of different thicknesses.

Sapphire, like crystalline quartz, is transparent in the THz range (Fig. 4d). Within the measurement accuracy, the transmittance of sapphire is independent of crystal orientation. For the measured samples with thicknesses from 1 to 5 mm, the transmittance below 600 μm is strongly dependent

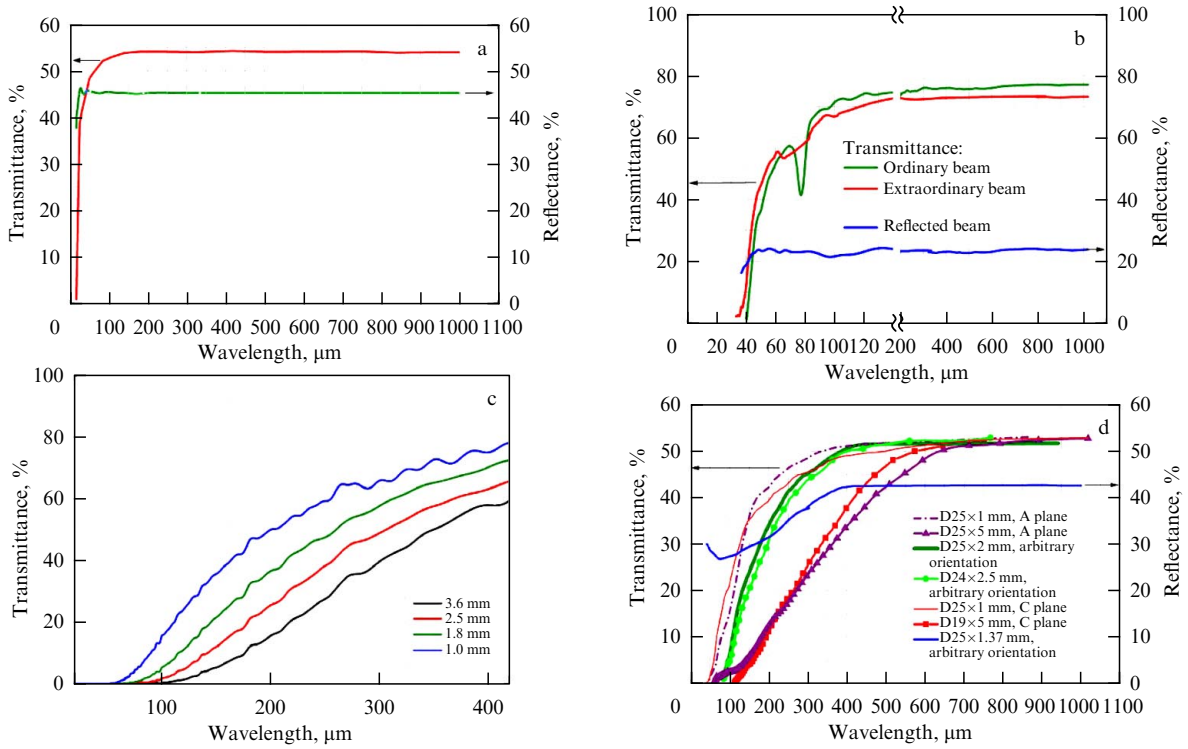

Figure 4. (a) Transmittance (red line) and reflectance (green line) spectra of 5 mm thick high-resistivity silicon in the THz range. (b) Transmittance spectra of 1 mm thick crystalline quartz. (c) Transmittance spectra of fused quartz plates KU1 with a thickness of (blue curve) 1 mm, (green curve) 1.8 mm, (red curve) 2.5 mm, and (black curve) 3.6 mm. (d) Transmittance spectra of sapphire plates of different thicknesses and crystallographic orientations (borrowed from [104]).

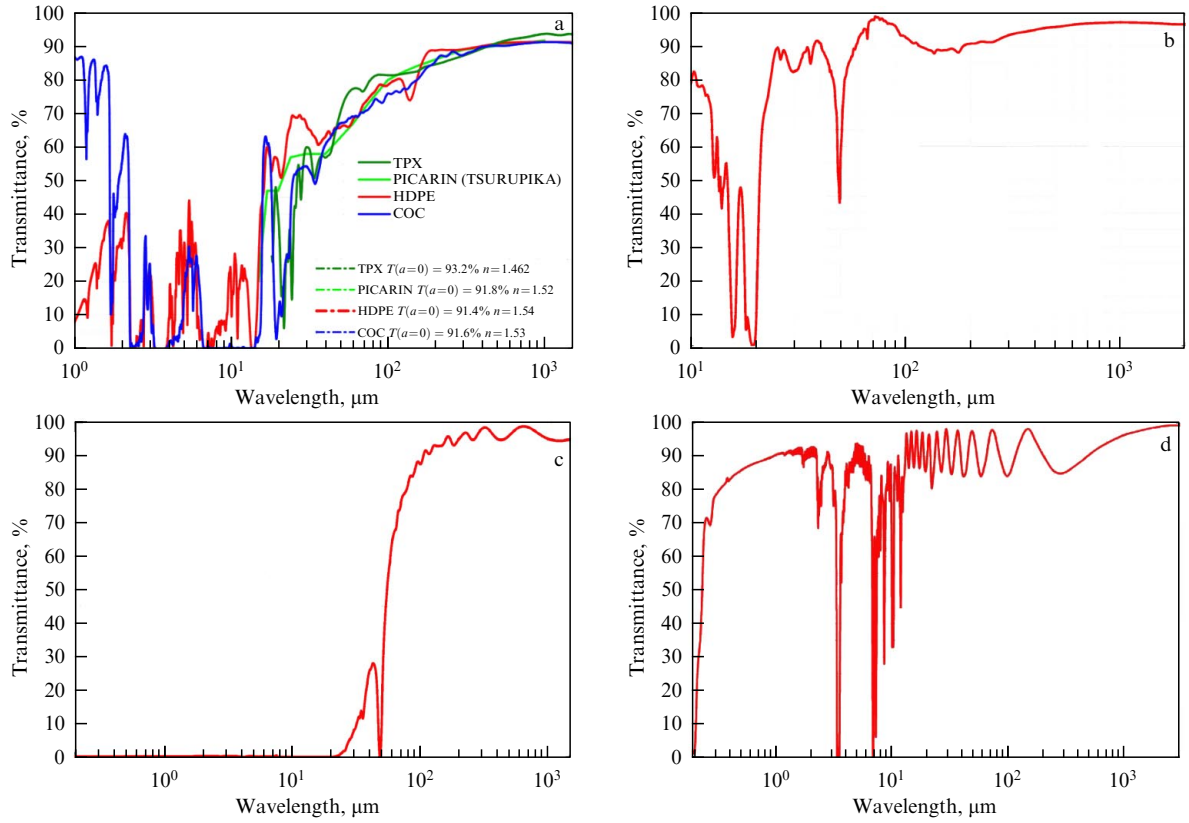

Figure 5. Transmittance spectra in the THz range: (a) TPX, picarin, HDPE, and COC (plate thickness 2 mm). (b) PTFE film (0.1 mm thick). (c) Zitex G11 film (0.25 mm thick). (d) Polypropylene film (0.05 mm thick). (Borrowed from [104, 105].)

on the sample thickness. At shorter wavelengths, transmittance tends to saturate for thinner samples.

In addition to crystalline materials, polymers are also used in THz optics. These include polymethylpentene, picarin (Tsurupica), cycloolefin polymer (Zeonex), cycloolefin copolymer (COC), polyethylene, polypropylene, and Teflon. At wavelengths of 200 μm and longer, the transmittance of all these polymers exceeds 80%. The first four polymers are also transparent in the visible range.

Polymethylpentene (TPX) is the lightest known polymer. It is transparent in the visible, IR, and THz ranges. Optical losses in the material remain very low down to millimeter wavelengths. TPX exhibits high thermal stability and resistance to a wide range of organic and inorganic substances. Its refractive index is close to 1.46 and is almost wavelength-independent. The transmittance spectrum of TPX is shown in Fig. 5a. Similar THz-transparent polymeric materials include picarin and cycloolefin polymers and copolymers; however, they are more expensive and less commercially available.

Polyethylene (PE) is another polymeric material transparent in the THz range. Depending on the grade, the thermal stability of polyethylene reaches 110 °C, allowing cooling to temperatures from −45 to −120 °C. Its refractive index is approximately 1.54 and varies slightly over a broad wavelength range. High-density polyethylene (HDPE) is commonly used for manufacturing optical components. Thin HDPE films are used in THz polarizers and filters and as windows for Golay cells. HDPE exhibits very low visible transmittance and therefore cannot be used for optical alignment in the visible range. The transmittance spectrum of a typical HDPE, together with those of COC and picarin, is shown in Fig. 5a. Black polyethylene containing graphite microparticles is typically used in THz filters. The transmittance of HDPE in the THz range is temperature-independent, making it suitable for use in cryostats.

Polytetrafluoroethylene (PTFE, Teflon, or fluoroplastic) is transparent in the THz range. It is a white, hard, and relatively dense plastic with a density of approximately 2.2 g cm^{-3} and a melting point of 327 °C. It retains its properties over a wide temperature range from −70 to 200 °C. With a refractive index of approximately 1.43 over a wide wavelength range, PTFE is widely used in the manufacture of THz filters. The transmittance spectrum of PTFE is shown in Fig. 5b. Porous PTFE with different average pore sizes is available under the Zitex product line (Fig. 5c). Polypropylene (PP) is also used in THz optics. It has a density of 0.9 g cm^{-3} and a refractive index of 1.49, slightly higher than that of polyethylene. Its melting point (170 °C) exceeds that of polyethylene, making PP more suitable for practical applications. Polypropylene is also more resistant to aggressive environments than polyethylene. The transmittance spectrum of PP is shown in Fig. 5d.

3.2 Cutoff filters

Cutoff filters transmit radiation with wavelengths either longer (blocking shorter wavelengths) or shorter (blocking longer wavelengths) than a specified cutoff. In the former case, they are referred to as high-pass filters (HPFs), and in the latter, low-pass filters (LPFs). The main characteristics of cutoff filters are the cutoff wavelength λ_c (the wavelength above which the transmittance of the filter exceeds the set threshold, often taken as 0.1%), the spectral slope $dT/d\lambda$, and the maximum T_m and background T_b tansmittances of the filter. The principal applications of THz cutoff filters include

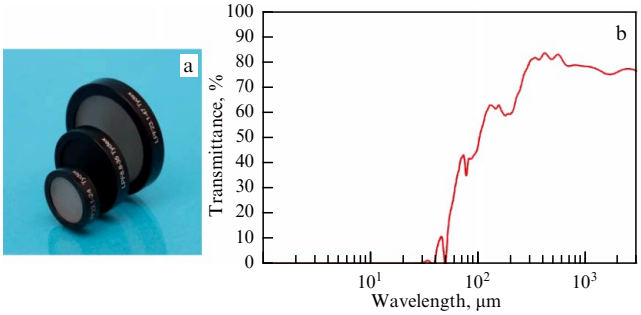

Figure 6. (a) External view of the THz cutoff filter. (b) Example of the transmittance spectrum of a THz cutoff filter with $\lambda_c = 47$ μm (borrowed from [16]). The filter materials used were 0.2 mm thick crystalline quartz, 0.05 mm thick polyethylene, and 0.25 mm thick Zitex.

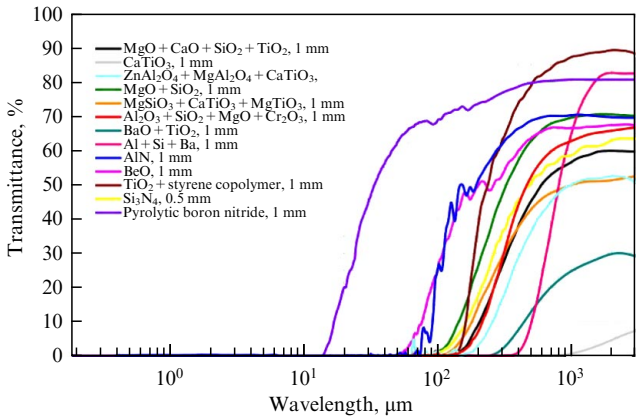

Figure 7. Transmittance spectra of several ceramic and solid materials in the THz range.

THz spectroscopy, imaging optics, terahertz diagnostic instruments, astronomy and astrophysics, material property research, sensors and detectors, and electro-optical research.

An example of cutoff filters based on assemblies of absorbing materials is provided by filters manufactured by Tydex LLC (Fig. 6a). These filters consist of multiple materials tightly mounted within a frame. The materials used in the manufacture of such filters are listed above in Section 3.1. They include flexible films (polyethylene, Teflon and its variety Zitex, polypropylene, etc.) or hard plates such as TPX, fused or crystalline quartz, as well as various plastics and ceramics (Fig. 7). Filters based on the latter typically cut off radiation at longer wavelengths and are suitable for operation at liquid-helium temperatures, which is important for astrophysical applications. They also exhibit a high damage threshold. As shown in Section 3.1, the maximum transmittance T_m for PE, Zitex (G11), TPX, and crystalline quartz, is 91.2, 98, 93, and 76.2%, respectively. By combining various absorbing materials, it is possible to obtain a specific edge of the THz transmittance spectrum λ_c within the range of 12 to 100 μm. An example of the transmittance spectrum of a real THz cut filter is shown in Fig. 6b.

4. THz filters based on metamaterials

Currently, quasi-optical resonant filters based on metamaterials (see Section 2.2 for details) are widely used in THz optics. These filters are made of thin metal foils patterned with periodically arranged holes of specific shapes [101, 106–112]. They provide a high degree of monochromaticity of the transmitted radiation while maintaining high source luminosity and are used, for example, in astrophysics polarimetry [113]. By selecting the shape of the holes, the thickness of the foil, and the relative position of the holes, it is possible to achieve a broad range of cutoff wavelengths and bandwidths. As discussed in Sections 2.2.2 and 2.2.3, a rigorous simulation of a resonant filter is possible by solving Maxwell's equations for all points around the filter cells, as well as by employing iterative machine-based algorithms. However, such methods are cumbersome. The problem is simplified by describing the filter response in terms of complex impedances $Z(f) = R(f) + iX(f)$, connected in parallel. Here, $R(f)$ and $X(f)$ are the functions of the active and reactive components of these impedances, respectively, determined empirically as functions of the shape of the holes (or islands), the filter design, and the material properties. In reality, the problem is further simplified if $R(f)$ and $X(f)$ are expressed in terms of the geometric parameters of the cells of the filters under study; i.e., the resonant frequency of the equivalent circuit is expressed in terms of the geometric parameters.

4.1 Geometries and equivalent circuits of FSSs used as real THz filters

The simplest THz filter based on an FSS is a strip grating filter (LPF or HPF). Strip grating filters are not widely used. The three most common classes of FSS-based filters used in THz optics are mesh filters (see Fig. 9, Section 4.1.1), cross-mesh filters (see Fig. 10a, b, Section 4.1.2), and filters with circular holes (or islands, Fig. 11b, Section 4.1.3). Mesh filters are advantageous because they are independent of the polarization of the incident radiation. Cross-mesh filters can be used as band-pass or notch filters (for a specific frequency band).

4.1.1 Strip grating filters. Mesh filters. Strip grating filters consist of a periodic array of equidistant thin metal strips. If the electric field vector **E** of the incident radiation is parallel to the metal strips, the filter is referred to as inductive. If the vector **E** is perpendicular to the strips, the filter is referred to as capacitive. A capacitive strip grating filter acts as a low-pass filter because it transmits only the wave with low-frequency oscillations **E**. The equivalent electrical circuit of a capacitive filter is shown in Fig. 8a. The incident high-frequency wave will induce current through the grounded capacitor, and therefore will be suppressed at the output port. If there is a low-frequency wave at the input, no current will arise through the capacitor, and, therefore, the wave will reach the output port. The equivalent circuit corresponding to the inductive filter geometry, on the contrary, is an inductor shunted to ground (Fig. 8b). Low-frequency radiation induces a current through a grounded inductor, while high-frequency radiation will not induce a current and will reach the output port. An inductive strip grating filter is a high-pass filter.

A major drawback of strip grating filters is their dependence on the polarization of the radiation. Next, we will consider filter geometries that are free of this drawback.

Schematic diagrams of inductive and capacitive mesh filters and their equivalent circuits are shown in Figs 9a and 9b. A capacitive mesh filter consists of an array of metal squares on a substrate transparent to a given radiation region, while an inductive mesh filter is a foil with square holes. Their transmittance is independent of the polarization of the radiation, which is evident if the polarization vector is expanded into basis vectors aligned with the sides of the

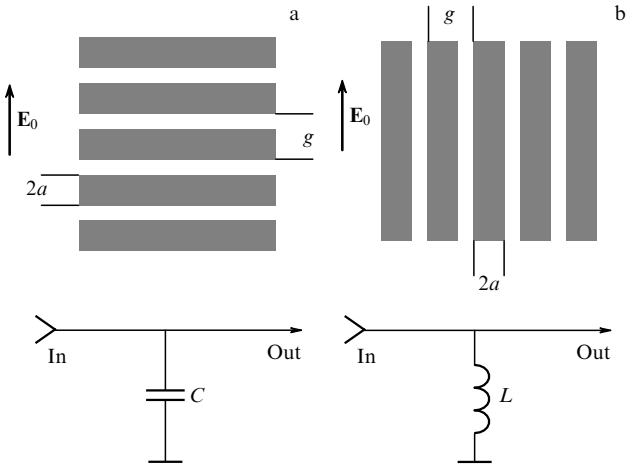

Figure 8. Equivalent circuits of (a) capacitive and (b) inductive mesh-strip filters.

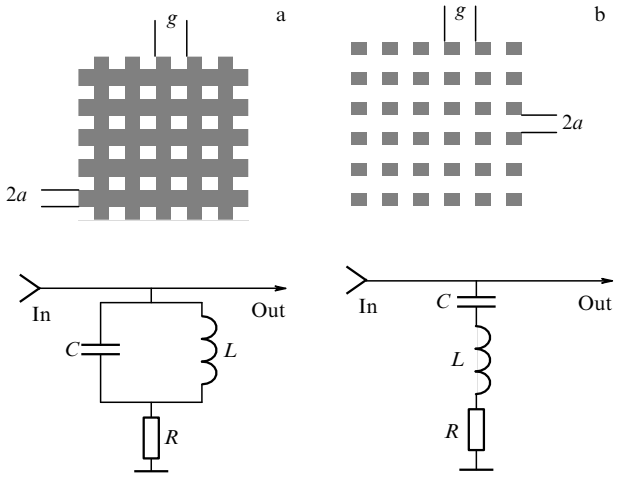

Figure 9. Equivalent circuits of (a) inductive and (b) capacitive mesh filters.

filter meshes. In the geometry of a capacitive mesh filter, charge carriers are limited to movement only within each individual square. These filters typically operate as notch filters. In the geometry of an inductive mesh filter, charge carriers are not confined within a single square and can traverse across the entire filter surface. Such filters function as bandpass filters. The reactances of their equivalent circuits (expressed in SI units) were determined empirically [114] as

$$X(f)_{\text{ind}} = \mu_0 g f \ln \csc \frac{\pi a}{g}\,, \tag{27}$$

$$X(f)_{\text{cap}} = -\frac{2\pi}{f\varepsilon_0\varepsilon_r}\left(\frac{2a}{g}\ln \csc \frac{\pi a}{g}\right)^{-1}, \tag{28}$$

where ε_0 and ε_r are the permittivities of vacuum and the medium, respectively; g and a are the geometric parameters of the filters shown in Fig. 9; c is the speed of light; and f is the frequency of the incident radiation. Equations (27) and (28) are applicable to both capacitive and inductive filters. Note that in some cases, reactances and admittances are expressed in normalized (dimensionless) form to simplify transmission-matrix calculations, as demonstrated previously in Section 2.2.2.

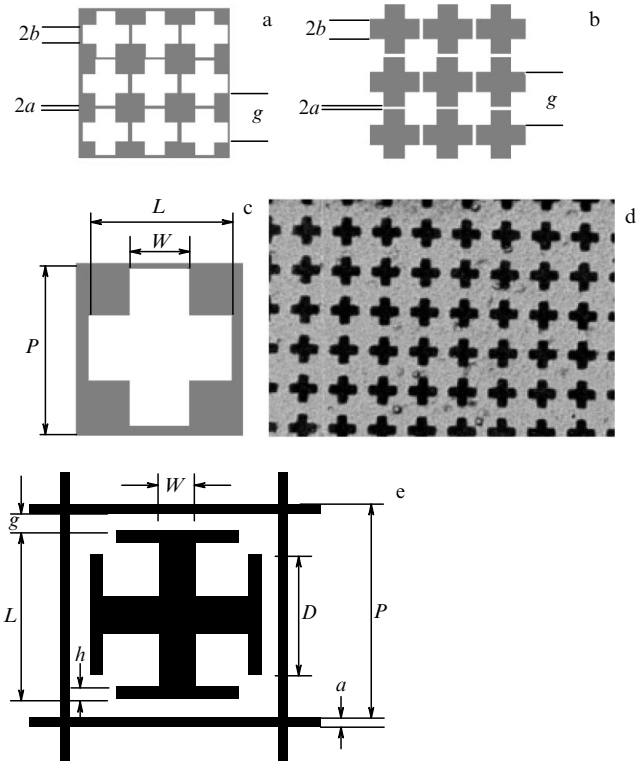

Figure 10. Schematic diagram of (a) bandpass inductive and (b) notch capacitive cross-shaped filters, (c) variant of geometric parameters, (d) micrograph of an inductive cross-shaped filter, and (e) geometry of the 'Jerusalem cross' mesh.

4.1.2 Cross-mesh filters. Another fundamental filter geometry is the cross-mesh configuration (Figs 10a and 10b). These filters are similar to mesh filters, but the repeating mesh element is a cross rather than a square. These filters are more efficient in terms of reducing the half-bandwidth and increasing the transmittance. The half-bandwidth of these filters typically ranges from 1 THz (for a passband centered at 10 THz) to 0.33 THz (for a passband centered at 1.5 THz) [109]. In the rejection region, the transmission of these filters is below 4% on both the short- and long-wavelength sides. The geometric dimensions of the crosses determine the resonant wavelength, which has zero transmittance for ideal capacitive filters and maximum transmittance for ideal inductive cross-mesh filters. The empirical formula for the resonant wavelength in terms of the geometric parameters a and b (Figs 10a and 10b) was obtained in [114]

$$\lambda_{\text{r}} = 2.27g - 4a - 2b\,. \tag{29}$$

An alternative empirical expression for λ_{r} is also used, defined in terms of other geometric parameters (Fig. 10c) of the filter: $\lambda_{\text{p}} = 2L - 1.35W + 0.2(P - L)$. This expression is close to, but not identical with, formula (29); there discrepancy between the resulting value of λ_{p} may arise from the differences in the initial approximations in the calculations. It was shown in [114] that the admittances of the two types of filters are expressed as

$$Y(f)_{\text{ind}} = \frac{1}{a_1 - \mathrm{i}gA_1/\left(\lambda_{\text{r}}\Omega(f)\right)}\,,$$
$$Y(f)_{\text{cap}} = \frac{1}{a_1 + \mathrm{i}gA_1/\left(\lambda_{\text{r}}\Omega(f)\right)}\,, \tag{30}$$

where a_1 and A_1 are the metal loss parameter and the parameter describing the passband, respectively. The values of these two parameters can be found empirically using the least-squares method. The normalized frequency function $\Omega(f)$ is defined as $\Omega(f) = \lambda_r f/c - c/\lambda_r f$. The characteristic size of an individual THz metamaterial 'pattern' element is several tens of micrometers. A micrograph of an inductive cross-shaped filter is shown in Fig. 10d. The transmittance of such filters reaches values up to 0.98 of the initial incident radiation intensity.

In general, any complex FSS can also be represented as a superposition of simple equivalent LC circuits. For example, a more complex capacitive cross-shaped mesh of the 'Jerusalem cross' type (Fig. 10d) can be described as a simple LC circuit (similar to that shown in Fig. 9b), for which the expressions given in [114] are valid:

$$\omega L \approx \frac{P}{\lambda} \ln\left(\frac{2P}{\pi W}\right), \qquad \omega C \approx \frac{4D}{\lambda} \ln\left(\frac{2P}{\pi g}\right). \tag{31}$$

4.1.3 Bandpass filters with circular holes (or islands). Inductive filters with circular holes (Figs 11a and 11b) have demonstrated comparable performance in terms of transmittance. The transmittance of these filters can also reach values up to 98% of the initial incident radiation intensity. The half-width of the passband of such filters is similar to that of filters with cross-shaped holes. In the suppression region, the transmittance of these filters reaches 15% on the short-wavelength side and 4% on the long-wavelength side.

For filters with circular holes, a simplified formula for the resonant wavelength of the central passband was derived [108]: $\lambda_r = g/0.85$. Researchers at Tydex LLC also proposed a refined empirical formula: $\lambda_r = 0.84g + 0.46D - 0.07t$, where g is the center-to-center spacing of the holes arranged at the vertices of a square, D is the hole diameter, and t is the filter thickness. For capacitive filters with circular islands, all the above considerations for capacitive cross-shaped filters are similar and valid.

When n identical filters are located in close proximity to each other (typically 3–5 mm), the transmittance of such a system is determined by the simple relationship $T = (T(\lambda))^n$ (Fig. 11c for $n = 2$). Figure 12 shows an example of the spectrum of a real inductive bandpass filter with cross-shaped holes.

Other hole geometries for THz filters are also known. For example, hexagon-shaped through-holes are described in [116]. In [117], in addition to square, circular, and cross-shaped holes, a number of other configurations are also presented, including three-pointed star geometries and grouped cross structures.

Ma et al. [118] described a so-called 'inverse double-humped' (i.e., two-band) capacitive THz filter based on a complex configuration consisting of an array of two nested crosses deposited on a high-resistance silicon substrate. This filter suppresses two spectral bands at frequencies of 2.6 and 4.37 THz. We again note the above comprehensive review devoted to the calculation of various FSS configurations [100].

The development of narrow-band bandpass filters has continued in recent years, as demonstrated in recent studies [119–122]. Liu et al. [121] reported numerical investigations of spectral features (modes) arising from broken symmetry in the configuration of cross-shaped resonators, which, according to the authors, gives hope for the development of ultra-narrow-band THz filters. Shahouvand et al. [122] focused on improving the design of narrow-band filters based on cross-shaped diaphragms.

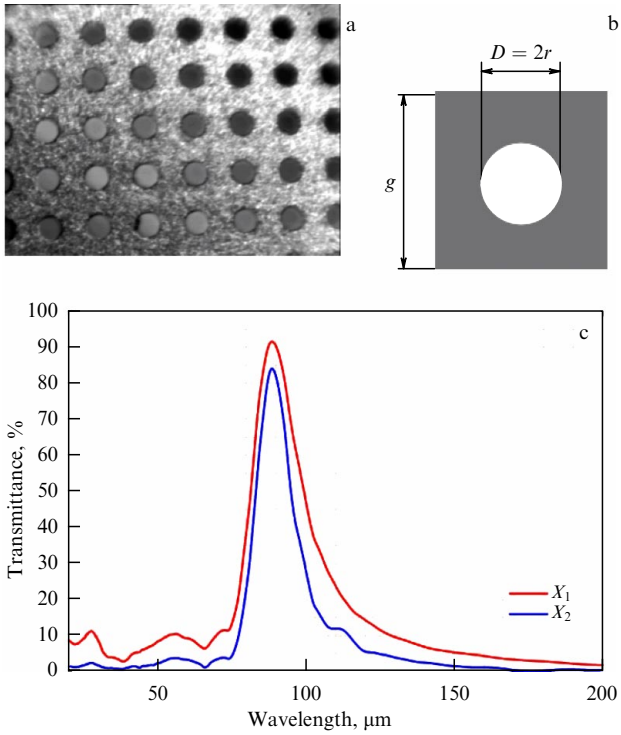

Figure 11. (a) Micrograph of an inductive bandpass filter with circular holes [110], (b) its geometric parameters. (c) Example of transmittance spectra of a single bandpass filter with round holes ($\lambda_r = 89$ μm, red curve) and two identical bandpass filters arranged in parallel (blue curve) [115] with parameters $g = 80$ μm, $D = 2r = 44$ μm, and $t = 10$ μm; the distance between filter layers is 0.5 mm.

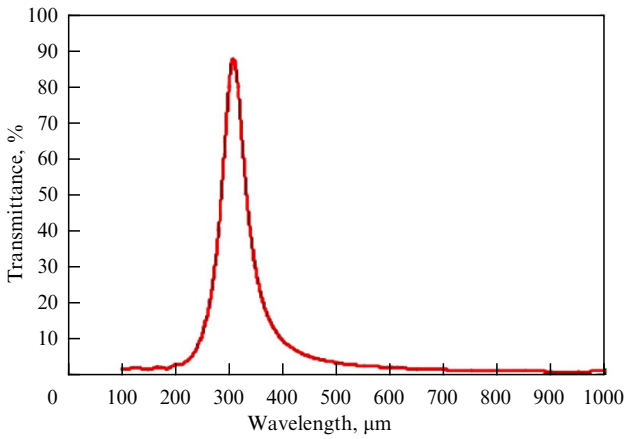

Figure 12. Example of a real transmittance spectrum of an inductive bandpass filter with $\lambda_p = 300$ μm (borrowed from [115]) with parameters $p = 200$ μm, $L = 160$ μm, $W = 20$ μm (an explanation of p, L, and W is given in Fig. 10c), and $t = 20$ μm (filter thickness).

Practical calculation of an FSS, in particular bandpass filters and their assemblies is carried out using machine methods and optimization algorithms. Calculation consists of two stages: (i) simulation of electromagnetic radiation propagation through the FSSs or their assembly (diffraction of a broadband cosine-modulated Gaussian pulse), and (ii) calculation of the parameters of the FSSs or their

assembly that provide the specified spectral characteristics of the system. When the required frequency distribution of wave energy is achieved, the calculations are completed. Otherwise, following the selected optimization method, the filter parameters are modified and the forward problem is solved iteratively.

4.2 THz notch filters

4.2.1 Filters based on split-ring microresonators. To enhance performance, a notch filter based on a two-layer metamaterial structure, originally developed for the microwave range, was used [123]. Due to the bilayer structure of the metamaterial, the filter demonstrates higher resonant absorption in reflection geometry compared to a simple capacitive mesh-based notch filter. A similar approach was later demonstrated for the THz range [124]. The unit cell of such a metamaterial (see the left side of Fig. 13a) consists of an electric split-ring resonator and a wire, separated by a dielectric layer (polyimide was used in [123]). Numerical simulations predicted almost 100% absorption for this cell. Experimentally, resonant absorption of 70% at 1.3 THz was demonstrated, which was attributed to fabrication inaccuracies (see the right panel of Fig. 13a). Absorption was subsequently increased experimentally to 97% in a flexible THz metamaterial, in which the wire was replaced by a gold grounded plate without a substrate [125, 126]. It was shown that such a filter can operate over a wide range of incidence angles. The transmittance spectra of these filters depend on the polarization of the incident radiation. Polarization-insensitive THz notch filters were also realized using more symmetric unit cell geometries [127, 128]. The operating principle of a double-layer notch filter is based on the coexistence of electric and magnetic responses, which can be independently tuned by modifying the geometry and thickness of the elements [123–125, 127]. A split-ring resonator strongly couples to the electric field and weakly to the magnetic field [79, 80], while the wire and the central part of the filter form a system that provides the magnetic response [82, 83]. In multilayer or bulk metamaterials treated as effective media, it is possible to fabricate filters whose impedance $Z = (\mu/\varepsilon)^{0.5}$ is matched to the impedance of the environment (vacuum), which leads to the absence of reflection. The filter parameters can be chosen so that the incident radiation is maximally absorbed. In this case, magnetic resonance plays a key role. However, such a filter behaves differently depending on the side from which the radiation is incident [129]. The filter cuts out the spectral band quite well if the radiation is incident on the ring resonator. At the same time, the filter exhibits reflective properties when the light is incident on a grounded plate. The absorption mechanism in two-layer metamaterials is usually analyzed using transmission line theory [130–132]. In this framework, the split-ring resonator and the wire (or ground plane) are electrically decoupled and associated with corresponding surface impedances, while the layer between them is simulated as an equivalent transmission line for a propagating wave. The calculations well reproduce the asymmetric absorption of this filter.

Terahertz notch filters can be used as radiation absorbers in the detection of THz or thermal radiation, for example, in bolometers for THz imaging applications [133, 134]. Broadband and multiband absorption was demonstrated in [135] and [136, 137], respectively.

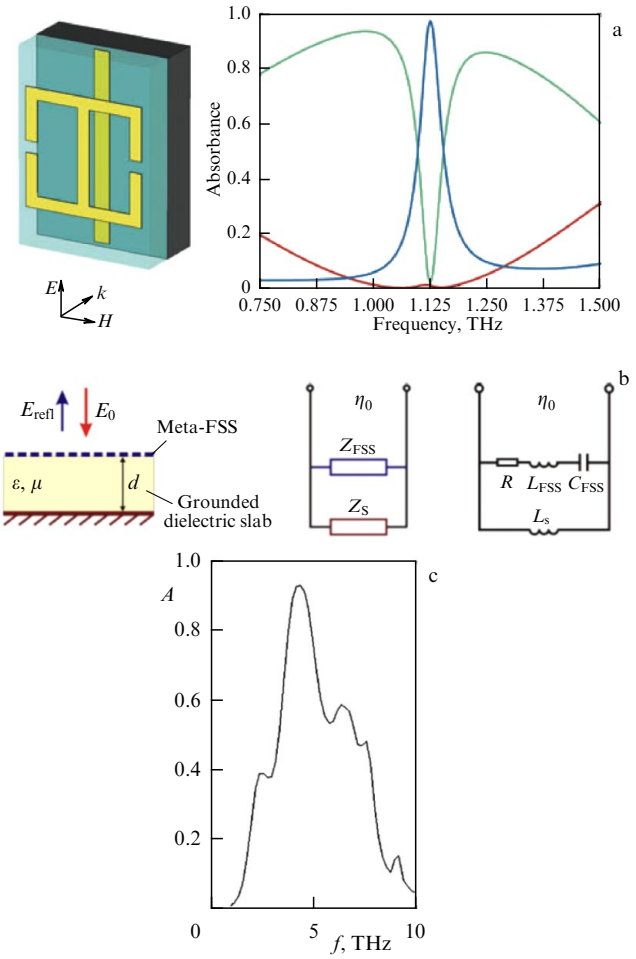

Figure 13. (a) Schematic of the unit cell of the two-layer THz notch filter (left) and the simulated spectra of the filter reflection (green curve), transmission (red curve), and absorption (blue curve) (right). (b) Schematic of the notch filter based on a high-impedance metamaterial, the equivalent circuit of the notch filter based on a meta-CSS and a grounded dielectric layer, and the *LCR* circuit representation for the capacitive-type meta-CSS notch filter (borrowed from [138]). (c) Spectral dependence of the absorbance of a microbolometric receiver with a metamaterial-based absorber (borrowed from [141]).

4.2.2 Filters based on the absorption of frequency-selective metamaterial surfaces. Terahertz radiation absorbers based on meta- and frequency-selective surfaces consist of two thin metal layers separated by a dielectric spacer. One layer is a solid metal that completely reflects radiation, and the second layer is a patterned FSS designed to provide a receiver impedance equal to that of a vacuum at specific frequencies. This eliminates the reflection of incident radiation, resulting in near-unity absorption. The approach to designing high-performance electromagnetic absorbers that demonstrate a significant excess of the operating wavelength range with a center wavelength λ over the absorber thickness d is based on controlling the spatial distribution of the electromagnetic field such that the maximum of the electric field is shifted to the absorber surface. This can be achieved using a so-called high-impedance surface (HIS) (see [138–140]). An electrically thin HIS is a subwavelength single-layer capacitive-type FSS (the so-called meta-FSS) placed above a thin grounded dielectric plate (see the left side of Fig. 13b).

At the resonant frequency of the HIS, the surface resistance tends to infinity, resulting in zero phase of the

reflected radiation. In this case, the tangential component of the total magnetic field formed by the incident and reflected waves vanishes at the HIS surface (the so-called 'magnetic wall' condition), while the electrical component reaches a maximum. By properly introducing dissipative losses in the dielectric plate, the perfect absorption regime can be realized in the system. If the dissipative parameter is chosen to be sufficiently small, the absorption resonance Q-factor and the λ/d ratio of the absorber can reach values of several hundred, which is attractive for spectrophotometric applications. In the equivalent circuit, the surface impedance of the HIS-based structure is considered [125] as a parallel connection of the meta-FSS impedance Z_{FSS} and the impedance Z_S of the grounded dielectric plate (see the middle panel of Fig. 13b):

$$Z = \frac{Z_{FSS} Z_S}{Z_{FSS} + Z_S} . \tag{32}$$

The amplitude reflection coefficient r, which tends to zero at the absorption resonant frequency, is generally related to Z by the relation

$$r = \frac{Z - \eta_0}{Z + \eta_0} . \tag{33}$$

The meta-FSS impedance can contain both inductive and resistive terms, along with the capacitive one. These terms are taken into account by introducing an inductance L_{FSS} and resistance R in series with a capacitance C_{FSS} (see the right side of Fig. 13b):

$$Z_{FSS} = R + i\left[\omega L_{FSS} - (\omega C_{FSS})^{-1}\right], \tag{34}$$

where ω is the angular frequency corresponding to the radiation frequency. For normal incidence, the impedance of the grounded plate is expressed in terms of the thickness d and the intrinsic resistance of the dielectric substrate $Z_0 = \eta_0(\mu/\varepsilon)^{0.5}$ (see [125, 139]):

$$Z_S = iZ_0 tgkd, \tag{35}$$

where $k = (\varepsilon\mu)^{0.5}\omega/c_0$ is the wave vector in the substrate with dielectric constant ε and magnetic permeability μ (we assume $\mu \cong 1$ at THz frequencies), c_0 is the speed of light in a vacuum, and η_0 is the vacuum impedance. Under the condition $d/\lambda \ll 1$, the plate impedance (35) reduces to a purely inductive form $Z_S \cong i\omega L_S$ with an effective inductance L_S proportional to the plate thickness d:

$$L_S \cong \frac{\mu\eta_0}{c_0} d . \tag{36}$$

The characteristics of an FSS-based notch filter depend significantly on the relationship between the inductance L_{FSS} and the plate inductance L_S. This relationship is expressed through the parameter

$$\xi = \frac{4L_{FSS}}{C_{FSS}\eta_0(\eta_0 - R)} ,$$

which takes into account that L_S (and, consequently, the absorber thickness d), satisfying the ideal absorption condition $\max(1 - |S_{11}|^2) = 1$, is a function of the circuit parameters L_{FSS}, C_{FSS}, and R. In [125], one can find the main characteristics of ideal ultrathin absorbers for various values of ξ, derived analytically from an equivalent circuit model for $R/\eta_0 \ll 1$. Tao et al. [125] showed that minimizing R is a decisive factor for maximizing the λ/d ratio of the absorber and for reducing the absorption bandwidth. As an example of the practical implementation, Kul'chitskii et al. [141] reported absorption exceeding 90% in the 5 THz region using an FSS-based filter.

4.3 Filters based on resonant switching by photoexcitation

Among THz metamaterials, a distinct class comprises the so-called resonantly switchable and frequency-tunable materials, in which semiconductors play a key role. The conductivity of these materials can be dynamically controlled through the photoexcitation of free charge carriers. The first dynamically switchable THz metamaterial using photoexcitation was demonstrated in [142], where a GaAs wafer served as the substrate for a planar array of single split-ring resonators. Photogenerated carriers were excited using femtosecond near-IR laser pulses, which increased the surface conductivity and, consequently, the losses in the GaAs substrate. The resonant response decayed sharply with decreasing current density of the photogenerated carriers; i.e., the transmittance of THz radiation changed most dramatically near resonant frequencies. Using the described material configuration, a dual-band THz notch filter was demonstrated (Fig. 14).

Dynamic switching (modulation) of THz radiation can be very rapid if the lifetime of photogenerated carriers is sufficiently short. In GaAs, the carrier lifetime is typically in the nanosecond range, which leads to relatively slow transition of the metamaterial to its resonant state [142]. Prasankumar et al. [143] demonstrated the possibility of using GaAs/ErAs nanoisland superlattices as substrates for the metamaterial, with the carrier lifetime in the substrates ranging from fractions of a picosecond to tens of picoseconds. Using a femtosecond laser pulse in such superlattices, Chen et al. [144] experimentally demonstrated ultrafast switching ($\sim$ 20 ps) between resonant states of a THz metamaterial and, accordingly, ultrafast transmission of THz radiation through this filter.

Azad et al. [145] used the same substrate to realize ultrafast inter-resonant switching of surface-plasmon-enhanced THz radiation in two-dimensional arrays of

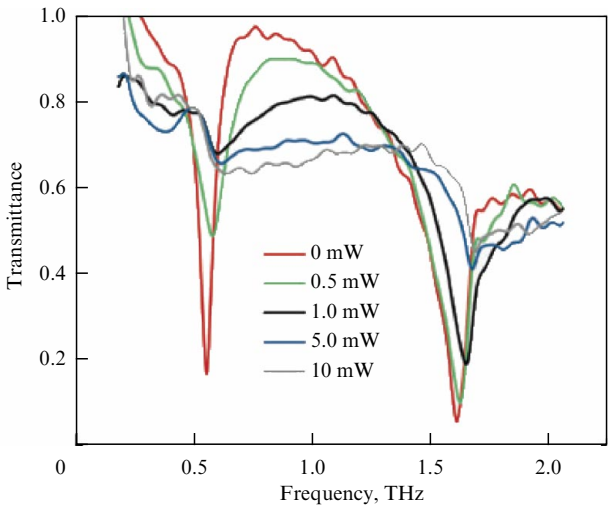

Figure 14. Transmittance spectra of an array of split-ring resonators on a GaAs substrate at different photoexcitation power levels (borrowed from [142]).

subwavelength metallic holes. Thus, by combining THz metamaterials with a semiconductor substrate, dynamic tuning of the resonant frequency of the metamaterial via photoexcitation became possible [146, 147], enabling the development of ultrafast switchable THz filters. In particular, Azad et al. [145] also described an array of split-ring resonators deposited on a silicon-on-sapphire substrate, in which the 0.6 μm-thick high-resistivity silicon layer was almost completely removed, leaving only two strips near the resonator slit. These strips became highly conductive under photoexcitation and effectively formed the capacitive plates of the capacitor. Changing the capacitance in the slit gap through photoexcitation shifted the resonant frequency of the metamaterial toward longer wavelengths (red shift) by more than 20%.

4.4 THz high-pass filters

Terahertz high-pass filters are designed to block low frequencies while transmitting high frequencies in the THz range. These filters are used in THz spectroscopy, astronomy and astrophysics, and THz sensing technology, and for isolating high harmonics of radiation generated by THz free-electron lasers. One implementation of these filters consists of a set of metal plates with subwavelength through-holes. Figure 15 shows the general appearance and transmittance spectrum of such a filter, in the form of a brass plate with a diameter $D = 20$ mm and a thickness $t = 1$ mm. The holes in the plate are square, with a side length $a = 0.3$ mm, and the width of the bridge between the holes is 0.1 mm. According to their operating principle, such devices belong to the class of waveguide high-pass filters where each microholes act as waveguides with a cutoff frequency determined by its geometry [148, 149].

The amplitude of the wave propagating through each waveguide is given by the expression [151]

$$|\mathbf{E}| = |\mathbf{E}_0| \exp\left[iz\left(\frac{2\pi}{\lambda}\right)\sqrt{\left(\frac{\lambda_c}{\lambda}\right)^2 - 1}\right], \qquad (37)$$

where $\mathbf{E}$ is the electric field at point z (the coordinate along the waveguide), and $\mathbf{E}_0$ is the field at the initial point (at the entrance to the waveguide). If $\lambda > \lambda_c$, the incident wave will decay exponentially along the waveguide, which determines its filter properties. The holes in the plate may be square or circular. The parameters of square high-pass filters are calculated using the formula $a = c/2f_c$, where c is the speed of light, $f_c = c/\lambda_c$ is the cutoff frequency, and a is the length of the side of the square. The period of the hole array, and therefore the width of the metal bridge between the holes, is chosen to be as small as possible. The bridge width is limited only by fabrication constraints. The bridge width does not affect the cutoff frequency position, but the larger its size, the lower the transmission in the working frequency range. The thickness of the metal plate is usually chosen to be at least 1 mm. According to the data from Tydex LCC [150], high-pass filters with transmittance below 0.1% in the cutoff region and cutoff frequencies up to 0.5 THz can be fabricated. A typical transmittance spectrum is shown in Fig. 15b for a filter with a cutoff frequency $f_c = 0.34$ THz. Filters with similar parameters are also fabricated by QMC Instruments Ltd. (United Kingdom) [152]. As an alternative to waveguide filters, a cascade of four to six bandpass filters can be used; however, their spectral characteristics are generally inferior [153].

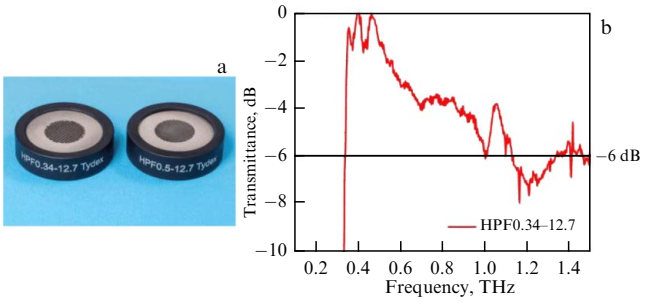

Figure 15. (a) General view of the high-pass filter, (b) characteristic transmittance spectrum (borrowed from [150]); cutoff frequency $f_c = 0.34$ THz.

4.5 Technologies for manufacturing metamaterials for THz filters and other FSS-based passive optical elements

The design, fabrication, and characterization of metamaterials operating in the microwave, THz, IR, and visible wavelengths are subject to different technological requirements. In THz metamaterials based on split-ring resonators or meshes with cross-shaped, circular, or square holes (or islands), the unit cell has external dimensions of several tens of micrometers ($\sim \lambda_0/10$, where λ_0 is the wavelength of the incident radiation in vacuum), while the smallest structural elements are on the micron scale. Therefore, planar THz metamaterials can be fabricated using conventional ultraviolet (UV) photolithography. Other fabrication methods for planar THz metamaterials (designed to operate at longer wavelengths) include conventional printing [154, 155] and inkjet printing [156]. Kaur et al. [157] demonstrated the possibility of using 3D printing technology to fabricate periodic structures suitable for THz filtering applications.

High-resistivity semiconductors or dielectrics are used as substrates for THz metamaterials. In addition to providing mechanical support, these substrates also affect the overall properties of the metamaterial, acting as elements of an equivalent electrical circuit. Terahertz metamaterials based on polymers and flexible silk-based films for biological and medical applications are described in [158–162].

Photolithography used for fabricating FSS-based filters is a well-established process [163] that typically involves six steps: (1) deposition of a metal film on the substrate, (2) spin-coating of a photoresist and installation of a photomask, (3) UV exposure, (4) photoresist removal, (5) etching of the metal film outside the area under the photoresist, and (6) photoresist rinsing and final cleaning.

Inductive bandpass resonant filters cab be also manufactured using a simpler technique — electroforming [164] from nickel foil, typically 3 μm thick. In this case, with optimal selection of geometric parameters (see Section 4.1.3), it is possible to fabricate filters with the transmittance exceeding 90% at λ_r. Other metals (for example, copper) may also be used for fabrication, although the minimum foil thickness must exceed 3 μm. Nickel is often preferred because filters made of this material have a high damage threshold (at an incident radiation intensity of about 110 W cm^{-2} at a thickness of 7 μm). Nickel films are produced by depositing nickel from an electrolytic solution onto a photomask. The technological process includes the following stages: (1) cleaning the photomask, (2) placing the photomask in a galvanic bath, (3) depositing a nickel film onto the photomask, (4) removing the nickel film from the photomask,

(5) washing the nickel film, and 6) mounting the filter into a supporting frame. According to the data from Tydex LLC [115], this method can be used to fabricate bandpass filters for any bandwidth in the range from 0.1 to 15 THz (i.e., from 3000 to 20 μm). Such filters typically provide high transmittance (60–90%) in the passband and low transmittance (< 4%) in the rejection bands, with the damage threshold of such filters in the frequency range of 0.1–15 THz being 65–100 W cm^{-2}.

The process of radiation transmission through planar (quasi-two-dimensional) metamaterials is more accurately described as a scattering process rather than propagation through an effective medium [165]; in the latter case, the formation of a three-dimensional structure is required. The fabrication of three-dimensional THz metamaterials remains technologically challenging. Quasi-three-dimensional THz metamaterials can be obtained by layer-by-layer fabrication or stacking of two-dimensional metamaterial layers [166–170]. One of the major challenges in producing true three-dimensional THz metamaterials is the fabrication of out-of-plane resonators, which is difficult to realize using standard microfabrication methods. One possible solution involves the use of microelectromechanical systems (MEMS) to fabricate reconfigurable THz metamaterials. For example, Tao et al. [171] described the fabrication of an array of free-standing out-of-plane split-ring resonators connected to a supporting substrate by cantilever-like legs. In their well-known work, Randhawa et al. [172] proposed a three-stage hierarchical self-assembly process for producing microarrays composed of metallic polyhedra. Another technique for fabricating 3D metamaterials has been demonstrated for applications in the mid-IR spectral range [173, 174], although it may be adapted for THz frequencies. The technique is based on membrane projection lithography, a multi-step process for fabricating out-of-plane split-ring resonators. First, a thin membrane material is deposited onto a relatively thick polymer film. Then, lithographic patterning is used to form holes in the membrane in the shape of split-ring resonators. These holes allow the developer to dissolve the underlying polymer, forming cavities beneath the membrane. Metals are then deposited through the holes to form out-of-plane split-ring resonators beneath the membrane and on the cavity walls.

Several studies have also reported other fabrication methods for THz metamaterials. Gentselev et al. [116] described a method for fabricating an all-metal high-pass filter using X-ray lithography to form an SU-8 photoresist mask on a silicon substrate with a tungsten photomask, followed by electroplating of a copper layer through a resistive mask. This method is based on the well-known method of fabricating similar structures using LIGA technology, where the sample is electroplated on the substrate through a resistive mask; however, it has several distinctions. Gentselev et al. [116] also proposed a new method for producing a high-contrast tungsten foil-based template. The topological pattern is created using photolithography and plasma-enhanced etching, which reduces the edge roughness of the template compared to laser cutting. The silicon substrate is removed by etching. Using the above technology, Gentselev et al. [116] fabricated a high-pass filter with a cutoff frequency of 0.42 THz.

Han et al. [175] reported the fabrication of bandpass cross-filters using laser ablation of microfoil. In the same work, pairs of these filters were used as Fabry–Perot etalons with tunable wavelengths.

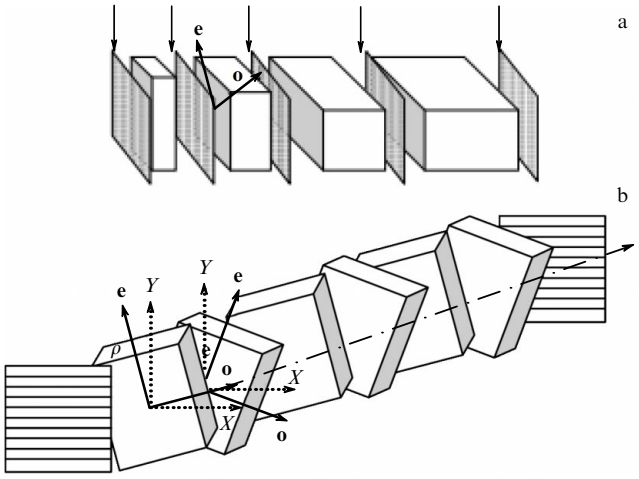

Figure 16. (a) Lyot polarization filter (borrowed from [182]). (b) Folded Scholz filter (borrowed from [196]).

5. THz polarization filters

Terahertz polarization filters [176] constitute a separate class of bandpass filters, whose operating principle is based on the birefringence effect and the absorption of polarized radiation in birefringent media. Polarization filters have been known for a long time and have been discussed in numerous works [177–193]. However, their application in the THz frequency range is a relatively new research direction. Two types of polarization filters are described in the literature: the Lyot filter [194] and the Solc filter. The Lyot filter consists of an assembly of wave plates of varying thickness with linear polarizers inserted between them (Fig. 16a (borrowed from [182])). Chen et al. [195] described a tunable THz Lyot filter operating in the frequency range of 0.388–0.564 THz using liquid crystal wave plates.

A Solc filter consists of a set of identical wave plates in which the directions of the optical axes alternate with the opposite sign at equal azimuthal angles ρ. The set is placed between crossed polarizers. There are two types of Solc filters. The first type is an alternating Solc filter [196], in which the angle of the kth plate $\phi_k = (-1)^k\rho$ ($k = 0, 1, \ldots,$ even) relative to the direction of polarization of the incident radiation (the polarization is formed after passing through the first, outer, polarizer) (Fig. 16b). The second type is a fan Solc filter, in which the optical axes of the wave plates are sequentially rotated by the same azimuthal angle $\phi_k = (2k + 1)\rho$, $k = 0, 1, \ldots$ The Lyot filter suppresses secondary maxima near the passband somewhat better than the Solc filter. However, the passband of the Solc filter is narrower, and its transmittance is higher [180]. There are known works describing tunable Solc filters based on controllable electro-optical wave plates [197] and liquid crystals [198, 199]. In the latter study, the filter operated within a passband of 0.176–0.793 THz and consisted of two controllable liquid crystal wave plates placed between two parallel wire polarizers.

A method for calculating an alternating Solc filter is presented in [193]. The center frequency f_c of the Solc filter is determined by the expression

$$f_c = \frac{(2m + 1)c}{2(n_e - n_o)d}, \qquad m = 0, 1, 2, 3, \ldots, \tag{38}$$

where n_e and n_o are the refractive indices of the extraordinary and ordinary waves, respectively; d is the thickness of the wave plate (identical for all plates); m is the order of the half-wave plate; and c is the speed of light in vacuum. The filter transmittance is derived using the Jones matrix method [200] and the Chebyshev identity [201]:

$$T = \left| \tan(2\rho) \cos\chi \, \frac{\sin(N\chi)}{\sin\chi} \right|^2 . \tag{39}$$

Here $\cos\chi = \cos(2\rho)\sin\Gamma/2$, where Γ is the frequency-dependent retardation (phase delay) of the wave plate, and N is an even number of wave plates. This expression can be simplified to $T = \sin^2(2N\rho)$ for $\Gamma = (2m+1)\pi$. Thus, the transmittance of the Solc filter at the center frequency f_c reaches 100% if $\rho = \pi/4N$.

More detailed calculation methods and examples of polarization filters based on the Jones formalism can be found, for example, in [180, 184, 202–208].

Additionally, it is worth mentioning the so-called tunable composite wave plate, which consists of an assembly of several wave plates of calculated thickness arranged at specific azimuthal angles [209, 210]. This device functions as a wave plate tuned to different frequency regions of the THz range. In the cited work, the possibility of using tunable composite wave plates as a nontunable Solc THz filter was demonstrated. The angles were calculated based on the theory described in [179], and the composite wave plate was sandwiched between a pair of crossed linear polarizers.

6. THz plasmonic filters

Attempts to develop THz filters based on plasmonic effects have been reported in the literature. Early studies [24, 211] also demonstrated the presence of a plasmonic response at frequencies of several GHz in thin metal wire structures, where the effective plasma frequency is much lower than that in bulk metals. The use of plasmonic metamaterials for THz applications as high-pass filters was also proposed in [212].

For bulk metals at $\omega t_c \gg 1$ (where t_c is the free-carrier relaxation time), the frequency-dependent dielectric constant is described by the Drude model as

$$\varepsilon(\omega) = 1 - \frac{\omega_p^2}{\omega^2} , \tag{40}$$

where ω_p is the plasma frequency, related to the electron density n, the electron mass m_e, and the charge e by the expression $\omega_p^2 = ne^2/\varepsilon_0 m_e$. For most metals, the plasma frequency lies in the visible to the ultraviolet ranges. The use of metamaterials allows the value of ω_p us to be reduced in the THz frequency range and also formula (40) to be applied to the THz range due to the satisfiability of the condition $\omega t_c \gg 1$. According to the theory presented in [24], for metamaterials consisting of a two-dimensional array of wires, the formula for the plasma frequency will be valid for their electromagnetic response to an incident wave with an electric field component parallel to the wires.

$$\omega_p^2 = \frac{2\pi c_0^2}{a^2 \ln(a/r)} , \tag{41}$$

where c_0 is the speed of light in vacuum, a is the lattice constant of the two-dimensional wire structure, and r is the wire radius. The plasma frequency decreases not only due to a decrease in the effective electron density but also due to an increase in the effective electron mass caused by the induced current in the wire and, consequently, an increase in the magnetic field around the wire. The effective plasma frequency depends significantly on the lattice constant and the wire radius. This fact makes it possible to tune ω_p by selecting the geometric parameters of the metamaterials. For electromagnetic waves with a frequency below ω_p, the effective dielectric constant of a thin metal structure will be negative, according to Eqn (40), and the wave will not propagate within the metamaterial. At frequencies above ω_p, the effective dielectric constant is positive, allowing the wave to propagate through the structure. The reflectivity for normal incidence of light on such a metamaterial can be calculated from the Fresnel equation

$$R = \left| \frac{\left(\dfrac{k_0/\varepsilon_0 - k_1/\varepsilon_1}{k_0/\varepsilon_0 + k_1/\varepsilon_1}\right)\left(1 - \exp(-2ik_1 d)\right)}{1 - \left(\dfrac{k_0/\varepsilon_0 - k_1/\varepsilon_1}{k_0/\varepsilon_0 + k_1/\varepsilon_1}\right)^2 \exp(-2ik_1 d)} \right|^2 , \tag{42}$$

where k_0, ε_0 and k_1, ε_1 are the wave vector and permittivity of air and the metamaterial, respectively; and d is the thickness of the metamaterial. The value of ε_1 depends on the frequency and can be calculated using Eqns (40) and (41). It has been shown that the behavior of R is characteristic of a high-pass filter. By varying the geometric parameters of the material, the transmission spectrum of filters of this type can be tuned.

A plasmonic bandpass filter is also described in [213]. This filter also consisted of an array of nanorods, providing zero transmission of radiation whose the electric field vector was parallel to the nanorods within a specific frequency range. The filter was fabricated using ultraviolet photolithography. The maximum filter transmittance reached 97.5%. Increasing the nanorod diameter was shown to shift the center frequencies of both the primary and secondary passbands of the filter toward higher frequencies. To model the filter, Gallant et al. [213] used finite-difference time domain (FDTD) simulations [214], analyzing the photonic band gap of the rod system. However, since no plasmonic edge is observed at the calculated frequency ω_p, it is possible that the filtering effect in this study arises from the photonic crystal effect rather than to a plasmonic mechanism.

7. Exotic THz filter

In addition to the THz filters used in THz optics and photonics and produced industrially (see Sections 3 and 4), a number of unconventional scientific approaches to THz filtering have also been reported, brought to the experimental stage. These approaches are currently of predominantly scientific rather than industrial value; nevertheless, such filters deserve special attention.

Gomon et al. [215] demonstrated that if a layer of carbon nanotubes is deposited onto a 'conventional' bandpass filter with cross-shaped holes, optical pumping with a 980 nm laser changes the magnitude of the primary transmission maximum of the filter, while the position of the secondary absorption maximum shifts to higher frequencies (by 9 GHz relative to 0.275 THz). This occurs because optical pumping changes the impedance of the surface with the deposited nanotubes, which also alters the conditions for the emergence of a resonant mode.

Odit et al. [216] described a THz tunable bandpass filter based on two parallel cross-hole meshes integrated with a nematic liquid crystal. By applying a control voltage to the liquid crystal, its permittivity — and therefore the overall transmittance of the system — changes. Odit et al. [216] also demonstrated a shift in the position of the passband maximum from 0.82 to 0.87 THz.

Several studies have reported tunable THz filters based on graphene-containing materials [217–219]. In particular, Li et al. [217] described a notch resonant filter based on doped graphene rings on a silicon substrate, whereas Mohammadi et al. [219] proposed a tunable resonant THz filter based on the Fano resonance with a controllable Fermi level position in a graphene-containing gel. Tian et al. [220] recently demonstrated a resonant THz high-pass filter using a periodic graphene-based grating representing a one-dimensional photonic crystal. A shift in the resonant frequency of the filter from 0.446 to 0.715 THz was achieved by using different replaceable graphene gratings.

Stecher et al. [221] described a type of a THz notch filter fabricated using a photonic crystal, which is an array of holes in a polymer tube made of TOPAS cycloolefin copolymer with low losses in the THz range. Yuan et al. [222] reported the fabrication of a notch filter based on a periodic system of holes in a polymer waveguide, where the transmittance spectrum of the filter exhibited a spectral dip 200 GHz wide, centered around 0.3 THz.

Lee et al. [223] demonstrated the effect of high-frequency filtering of THz radiation for TE modes. The TM_0-, TM_2- and TM_4-modes generated in a system of parallel plates with a frequency of 4 THz were used for filtering their low-frequency components, and the radiation of the TE_1 mode was cut off at a frequency of 1.5 THz in the case of mutually parallel orientation of the mode polarization and the plane of the plates.

Wang et al. [224] described a bandpass interference filter based on an array of silicon microdisks in a TPX polymer matrix. They showed the dependence of the transmittance spectrum of this filter on the radius of the microdisks and demonstrated a shift of the passband by 0.3 THz in the 1–1.5 THz region. The operating principle of the filter relies on the resonant effect of wave absorption in periodic structures based on materials with different refractive indices, such as photonic crystals. Filtering of THz radiation in such systems was previously described in [225].

Beheshti et al. [226] discussed a THz bandpass filter based on multilayer metamaterials and performed numerical simulations and experimental verification of its operation. First, they studied the behavior of a two-layer metasurface, which is a periodic structure with two-layer cylindrical unit cell. The authors then showed that increasing the number of cylinders as basic elements in the unit cell increases the bandwidth of the filter passband. Furthermore, the possibility of tuning the center frequency by varying the size of the basic element was demonstrated. The main advantages of the proposed structure are its wide bandwidth, tunability, and ease of assembly. The passband of the proposed filter was shown to be approximately 1 THz, and the transmittance was close to 93%. The original idea was based on work [227], which described the possibility of fabricating an assembly of several resonators based on metamaterials to create a resonant supercell.

Chen et al. [228] presented a model of a switchable notch/cutoff filter based on a vanadium oxide (VO_2) metamaterial. This metamaterial undergoes a phase transition between conducting and insulating states at 67 °C, allowing thermal control of its properties. The authors described a multilayer assembly consisting of a VO_2 interlayer enclosed in an Si_3N_4 layer deposited on a silicon substrate. An aluminum control contact was deposited onto the VO_2 surface. When VO_2 is in the insulating state, the assembly acts as a notch filter with a center frequency of 0.95 THz, and when VO_2 undergoes a transition to the metallic state, the filter acts as a cut-off filter.

Terahertz-range tunable filters based on MEMS technology are described in [229–232]. The bandpass filter described in these papers was developed using a photonic crystal (a mechanically tunable assembly of two lattice metal plates), providing tuning in the 3.5 GHz range. Another variant of a tunable bandpass THz filter based on a photonic crystal is the assembly [233] based on a pair of Bragg mirrors consisting of three crystalline quartz plates interleaved with two CeO_2 ceramic layers. A single crystal of $SrTiO_3$ was placed between the mirrors, providing tuning of the filter parameters due to the temperature dependence of the dielectric constant. Unfortunately, MEMS-based devices are complex and expensive to manufacture, and generally have a low quality factor.

An exotic variant of a bandpass THz filter is the interference filter based on a periodic structure, described in [234]. This filter is an assembly of repeatedly alternating plates of two materials with different refractive indices. One of the two materials is a quarter-wave plate with a refractive index of n_2. The quarter-wave plate is placed between two groups of layers $(n_1n_2)^N(n_1n_2)^N$, resulting in an assembly $(n_1n_2)^N n_2 (n_1n_2)^N$, where N is the periodicity (Fig. 17), and l_1 and l_2 are the thicknesses of the corresponding plates. If a plate of material n_2 is placed on the right side of the sequence and the assembly itself is placed between substrates with refractive indices n_a and n_b (preferably equal), the transmission of the assembly will behave equivalently to a bandpass filter around a certain wavelength λ_0.

The reflective regions of the dielectric mirror are determined by the N-fold periodic repetition of the assemblies $(n_1n_2)^N$. The transmission matrix for the total electric and magnetic fields of the ith layer is determined by the expression

$$\begin{bmatrix} E_j \\ H_j \end{bmatrix} = M_i \begin{bmatrix} E_{j+1} \\ H_{j+1} \end{bmatrix} \quad j = N, N-1, \ldots, 1\,, \tag{43}$$

where

$$M_j = \begin{bmatrix} \cos(k_j l_j) & \mathrm{i}\eta_i \sin(k_j l_j) \\ \mathrm{i}\eta_i \sin(k_j l_j) & \cos(k_j l_j) \end{bmatrix},$$

$k_j l_j = 2\pi n_j l_j/\lambda$, $\eta_j = \eta_0/n_j$, and η_0 is the wave impedance. The full transmission matrix can then be obtained by multiplying

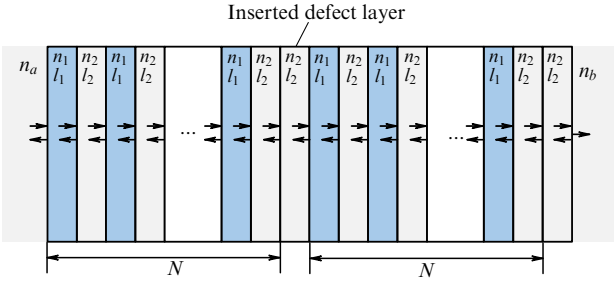

Figure 17. Schematic diagram of an interference THz bandpass filter based on a periodic array of double-stacked metamaterial layers.

all the transmission matrices of the layers in the assembly:

$$M = (M_1 M_2)^N = \begin{bmatrix} M_{11} & M_{12} \\ M_{21} & M_{22} \end{bmatrix}. \quad (44)$$

The reflectance and transmittance can be obtained from the formulas:

$$\begin{cases} r = \dfrac{(M_{11} + M_{12}\eta_0)\eta_0 - (M_{21} + M_{22}\eta_0)}{(M_{11} + M_{12}\eta_0)\eta_0 + (M_{21} + M_{22}\eta_0)}, \\ t = \dfrac{2\eta_0}{(M_{11} + M_{12}\eta_0)\eta_0 + (M_{21} + M_{22}\eta_0)}, \end{cases} \quad (45)$$

and the final transmittance of the assembly will be determined by the simple relationship $T = tt^*$. The authors present simulation results for $n_1 l_1 = n_2 l_2 = \lambda_0/4$ for a certain desired wavelength λ_0. The following values were chosen: $n_a = n_b = 1.52$ (glass), $n_1 = 2.1$ (zirconium oxide), and $n_2 = 1.4$ (magnesium fluoride). The wavelength $\lambda_0 = 1$ mm was also chosen to be 1 mm, corresponding to a frequency of 0.3 THz, used in the telecommunications range. It was shown that by selecting the thickness and period of the layers, high accuracy and a narrow bandwidth of the transmission maximum can be achieved. In particular, with a 2% plate thickness deviation, the passband position accuracy is approximately 5%. The theory of interference amplification for filtering as applied to bandpass and other filters is also described in [235, 236] without regard to the specific frequency range and can be applied to the THz range with the selection of appropriate materials. However, to obtain practically significant filters using this method, extremely high precision is required in the manufacture of the plates in terms of thickness, parallelism, and minimal roughness, which reduces the practical significance of this type of filter.

Also noteworthy are papers [237, 238]. The authors describe the design of a filter that utilizes the frequency dependence of the phase velocity of the lowest order transverse-electric TE_1 mode of a waveguide located between a pair of reflective plates. The authors showed that this frequency dependence can be used as a basis for constructing a two-dimensional artificial dielectric medium with an effective refractive index $0 \leqslant n < 1$. In this case, the THz wave propagating inside the waveguide was refracted in the same way as in a conventional dielectric prism. This device made it possible to isolate radiation at a specific frequency within a broadband THz pulse. Since different frequency components have different refractive indices inside the waveguide, the propagation direction of these components inside the waveguide depends on the frequency according to Snell's law. Because the refractive index varied monotonically from one to zero with decreasing frequency, the beam emerging from the waveguide was spatially distributed across frequencies (chirped), with the high-frequency components of the radiation lying closer to the input optical axis and the low-frequency components being offset from the optical axis. The spatially distributed beam was then focused and coupled into an identical waveguide. This reversed the spatial chirp, recombining the various frequency components into a single output beam. By choosing the correct spacing between the plates, the waveguide length, and the angular position of the plates, various spectral filtering functions can be performed, blocking portions of the spatially chirped beam. For example, by placing a metal plate within the waveguide, the system acquires the properties of a low-pass filter. The authors also demonstrated the feasibility of such a system as a high-pass, band-pass, and low-pass filter in the 0.1–1 THz range. In general, the theory of resonant amplification, regardless of the specific frequency range, has been developed in a number of studies, for example [235, 236], and can be applied to the THz range with the selection of appropriate materials.

Thus, numerous studies are devoted to filtering THz radiation using various methods, including exotic approaches. This topic remains extremely relevant due to the development of instrumentation — THz radiation sources and detectors.

8. Conclusions

This review provides a detailed examination of passive optical elements for filtering THz radiation. It has been shown that filtering is possible based on several different physical principles: absorption and scattering in materials, and the use of frequency-selective surfaces that suppress transmitted radiation at specific frequencies. Filters in which incident light interacts with free carriers, causing surface plasmon resonances, filters based on birefringent media, and other exotic approaches to THz filtering have also been considered. References to a significant number of studies on this topic have been provided, demonstrating that the need for practical and easy-to-manufacture THz filters still remains, and research in this field is ongoing. The most widely used are cutoff filters based on a combination of layers of absorbing materials, as well as bandpass filters based on perforated metal foils. Terahertz filters are an integral part of THz spectroscopy and sensing devices. Interest in these areas of THz optics remains high.

It can be assumed that the further development of THz optical filter elements will be associated with improved manufacturing technology for frequency-selective surfaces, including increased fabrication accuracy and improved repeatability of array elements. The use of new absorbing materials with increased transmittance in the required THz radiation region is also possible. Algorithms for calculating THz filters have been developed and are well known. Work on exotic devices for filtering THz radiation will also continue, but in the near future their results are unlikely to become commercially significant.

References

1. Federici J F et al. *Semicond. Sci. Technol.* **20** S266 (2005)
2. Friederich F et al. *IEEE Trans. Terahertz Sci. Technol.* **1** 183 (2011)
3. Ajito K, Ueno Y *IEEE Trans. Terahertz Sci. Technol.* **1** 293 (2011)
4. Humphreys K et al., in *Proc. of the 26th Annual Intern. Conf. of the IEEE Engineering in Medicine and Biology Society, San Francisco, CA, USA, 1–5 September 2004* (Piscataway, NJ: IEEE, 2005) DOI:10.1109/IEMBS.2004.1403410
5. Zhang X-C, Xu J *Introduction to THz Wave Photonics* (New York: Springer, 2010) p. 49, DOI:10.1007/978-1-4419-0978-7_3
6. Jepsen P U, Cooke D G, Koch M *Laser Photon. Rev.* **5** 124 (2011)
7. Averitt R D, Taylor A J *J. Phys. Condens. Matter* **14** R1357 (2002)
8. Taylor Z D et al. *IEEE Trans. Terahertz Sci. Technol.* **1** 201 (2011)
9. Nuss M C, Orenstein J, in *Millimeter and Submillimeter Wave Spectroscopy of Solids* (Topics in Applied Physics, Vol. 74, Eds G Grüner) (Berlin: Springer, 2007) p. 7, DOI:10.1007/BFb0103419
10. Ashcroft N W, Mermin N D *Fizika Tverdogo Tela* (Moscow: Mir, 1979); Translated from English: *Solid State Physics* (New York: Holt, Rinehart and Winston, 1976)
11. van Exter M, Grischkowsky D *Phys. Rev. B* **41** 12140 (1990)
12. Piccioli N et al. *Appl. Opt.* **16** 1236 (1977)
13. Ghosh G *Handbook of Refractive Index and Dispersion of Water for Scientists and Engineers* (Brisbane: S. Ghosh, 2005); Available online, https://refractiveindex.info/?shelf=3d&book=liquids&page=water

14. Banda E J K B et al. *J. Phys. C* **20** 2323 (1987)
15. Benford D J, Gaidis M C, Kooi J W *Appl. Opt.* **42** 5118 (2003)
16. THz Low Pass Filters. TYDEX. Available online, https://www.tydexoptics.com/products/thz_assemblies/thz_low_pass_filter/
17. Shen Y C, Taday P F, Pepper M *Appl. Phys. Lett.* **92** 051103 (2008)
18. Franz M, Fischer B M, Walther M *Appl. Phys. Lett.* **92** 021107 (2008)
19. Kock W E *Bell Syst. Tech. J.* **27** (1) 58 (1948)
20. Jones S S D, Brown J *Nature* **163** 324 (1949)
21. Brown J *Proc. IEEE* **97** 45 (1950)
22. Rotman W *IRE Trans. Antennas Propag.* **10** 82 (1962)
23. Pendry J B et al. *Phys. Rev. Lett.* **76** 4773 (1996)
24. Pendry J B et al. *J. Phys. Condens. Matter* **10** 4785 (1998)
25. Pendry J B et al. *IEEE Trans. Microwave Theory Tech.* **47** 2075 (1999)
26. Smith D R et al. *Phys. Rev. Lett.* **84** 4184 (2000)
27. Shelby R A, Smith D R, Schultz S *Science* **292** 77 (2001)
28. Veselago V G *Sov. Phys. Usp.* **10** 509 (1968); *Usp. Fiz. Nauk* **92** 517 (1967)
29. Schurig D et al. *Science* **314** 977 (2006)
30. Schurig D, Pendry J B, Smith D R *Opt. Express* **14** 9794 (2006)
31. Alù A, Engheta N *Phys. Rev. E* **72** 016623 (2005)
32. Milton G W, Nicorovici N-A P *Proc. R. Soc. London A* **462** 3027 (2006) DOI:10.1098/rspa.2006.1715
33. Nachman A I *Ann. Math.* **128** 531 (1988)
34. Gbur G *Prog. Opt.* **45** 273 (2003)
35. Greenleaf A, Lassas M, Uhlmann G *Physiol. Meas.* **24** 413 (2003)
36. Greenleaf A, Lassas M, Uhlmann G *Math. Res. Lett.* **10** 685 (2003) DOI:10.4310/MRL.2003.v10.n5.a11
37. Cummer S A et al. *Phys. Rev. E* **74** 036621 (2006)
38. Greegor R B et al. *Appl. Phys. Lett.* **87** 091114 (2005)
39. Driscoll T et al. *Appl. Phys. Lett.* **88** 081101 (2006)
40. Justice B J et al. *Opt. Express* **14** 8694 (2006)
41. Rybin M V et al. *Sci. Rep.* **5** 8774 (2015)
42. Gaillot D P, Croënne C, Lippens D *Opt. Express* **16** 3986 (2008)
43. Leonhardt U *Science* **312** 1777 (2006)
44. Shalaev V M *Science* **322** 384 (2008)
45. Leonhardt U *New J. Phys.* **8** 118 (2006)
46. Ramakrishna S A, Pendry J B *Phys. Rev. B* **67** 201101 (2003)
47. Schurig D et al. *Science* **314** 977 (2006)
48. Schurig D et al. *Opt. Express* **15** 14772 (2007)
49. Rahm M et al. *Phys. Rev. Lett.* **100** 063903 (2008)
50. Zhang P, Jin Y, He S *Opt. Express* **16** 3161 (2008)
51. Kildishev A V, Shalaev V M *Opt. Lett.* **33** 43 (2008)
52. Narimanov E E, Shalaev V M *Nature* **447** 266 (2007)
53. Kildishev A V, Shalaev V M *Phys. Usp.* **54** 53 (2011); *Usp. Fiz. Nauk* **181** 59 (2011)
54. Lu X et al. *Front. Phys.* **10** 1 (2022)
55. Cao L et al. *Adv. Mater. Technol.* **10** 2401358 (2024) DOI:10.1002/admt.202401358
56. Cong L, Singh R "Sensing with THz metamaterial absorbers," arXiv:1408.3711
57. Prasad T et al. *Opt. Lett.* **32** 683 (2007)
58. Pendry J B *Phys. Rev. Lett.* **85** 3966 (2000)
59. Podolskiy V A, Narimanov E E *Phys. Rev. B* **71** 201101 (2005)
60. Podolskiy V A, Alekseyev L V, Narimanov E E *J. Mod. Opt.* **52** 2343 (2005)
61. Wangberg R et al. *J. Opt. Soc. Am. B* **23** 498 (2006)
62. Podolskiy V A, Narimanov E E *Opt. Lett.* **30** 75 (2005)
63. Durant S et al. *J. Opt. Soc. Am. B* **23** 2383 (2006)
64. Liu Z et al. *Nano Lett.* **7** 403 (2007)
65. Liu Z et al. *Opt. Express* **15** 6947 (2007)
66. Lee H et al. *Opt. Express* **15** 15886 (2007)
67. Pendry J B, Ramakrishna S A *J. Phys. Condens. Matter* **14** 8463 (2002)
68. Shalaev V M *Nature Photon.* **1** 41 (2007)
69. Wood B *Laser Photon. Rev.* **1** 249 (2007)
70. Goussetis G, Feresidis A P, Harvey A R *J. Mod. Opt.* **57** 1 (2010)
71. Cai W, Shalaev V *Optical Metamaterials: Fundamentals and Applications* 1st ed. (New York: Springer-Verlag, 2010) DOI:10.1007/978-1-4419-1151-3
72. Smith D R et al. *Phys. Rev. Lett.* **84** 4184 (2000)
73. Shelby R A, Smith D R, Schultz S *Science* **292** 77 (2001)
74. Yen T J et al. *Science* **303** 1494 (2004)
75. Moser H O et al. *Phys. Rev. Lett.* **94** 063901 (2005)
76. Katsarakis N et al. *Opt. Lett.* **30** 1348 (2005)
77. Azad A K, Dai J, Zhang W *Opt. Lett.* **31** 634 (2006)
78. Schurig D, Mock J J, Smith D R *Appl. Phys. Lett.* **88** 041109 (2006)
79. Chen H-T et al. *Opt. Express* **15** 1084 (2007)
80. Padilla W J et al. *Phys. Rev. B* **75** 041102 (2007)
81. Azad A K et al. *Appl. Phys. Lett.* **92** 011119 (2008)
82. Shalaev V M et al. *Opt. Lett.* **30** 3356 (2005)
83. Zhang S et al. *Phys. Rev. Lett.* **95** 137404 (2005)
84. Dolling G et al. *Science* **312** 892 (2006)
85. Dolling G et al. *Opt. Lett.* **30** 3198 (2005)
86. Gundogdu T F et al. *Opt. Express* **16** 9173 (2008)
87. Awad M, Nagel M, Kurz H *Opt. Lett.* **33** 2683 (2008)
88. Paul O et al. *Opt. Express* **16** 6736 (2008)
89. Beruete M, Sorolla M, Campillo I *Opt. Express* **14** 5445 (2006)
90. Croënne C et al. *Appl. Phys. Lett.* **94** 133112 (2009)
91. Wang S et al. *Appl. Phys. Lett.* **97** 181902 (2010)
92. Wang S et al. *J. Appl. Phys.* **107** 074510 (2010)
93. Ishikawa A et al. *Phys. Rev. Lett.* **102** 043904 (2009)
94. Tavallaee A A et al. *IEEE J. Quantum Electron.* **46** 1091 (2010)
95. Linden S et al. *Science* **306** 1351 (2004)
96. Zhou J et al. *Phys. Rev. Lett.* **95** 223902 (2005)
97. Chen H-T et al. *Laser Photon. Rev.* **5** 513 (2011)
98. Sternberg O "Resonances of periodic metal-dielectric structures at the infrared wavelength region," PhD Dissertation (Newark, NJ: New Jersey Institute of Technology, 2002); Available online, https://digitalcommons.njit.edu/dissertations/548
99. Russer P "The transmission line matrix method," in *New Trends and Concepts in Microwave Theory and Technics* (Trivandrum, India: Research Signpost, 2004)
100. Munk B A *Frequency Selective Surfaces: Theory and Design* (New York: John Wiley and Sons, 2000)
101. Ade P et al. *Proc. SPIE* **6275** 62750U1 (2006)
102. Leipoldt K J et al. *Int. J. Infrared Millimeter Waves* **12** 263 (1991)
103. Mittra R, Chan C H, Cwik T *Proc. IEEE* **76** 1593 (1988)
104. THz Materials. TYDEX. Available online, https://www.tydexoptics.com/products/thz_optics/thz_materials/
105. Rogalin V E, Kaplunov I A, Kropotov G I *Opt. Spectrosc.* **125** 1053 (2018); *Opt. Spektrosk.* **125** 851 (2018)
106. Ulrich R *Infrared Phys.* **7** 37 (1967)
107. Porterfield D W et al. *Appl. Opt.* **33** 6046 (1994)
108. Irwin P G J et al. *Infrared Phys.* **34** 549 (1993)
109. Melo A M et al. *Appl. Opt.* **47** 6064 (2008)
110. Kuznetsov S A et al. *Key Eng. Mater.* **437** 276 (2010)
111. Baumann F et al. *Opt. Lett.* **28** 938 (2003)
112. Winnewisser C et al. *Appl. Opt.* **38** 3961 (1999)
113. Bortolucci E et al., in *Proc. of the II Workshop on Semiconductors and Micro and Nano Technology, Seminatec, Sao Bernardo do Campo, Brazil, 2012*
114. Harvey A F *Tekhnika Sverkhvysokikh Chastot* (Moscow: Sov. radio, 1965); Translated from English: *Microwave Engineering* (London: Academic Press, 1963); Marcuvitz N *Waveguide Handbook* (New York: McGraw-Hill, 1951)
115. THz bandgap resonance filters. TYDEX. Available online, https://www.tydexoptics.com/ru/products/tgc-ustrojstva/thz_band_pass_filter/
116. Gentselev A N et al. *Optoelectron. Instrum. Data Proces.* **55** 115 (2019) DOI:10.3103/S875669901902002X; Translated from Russian: *Avtometriya* **55** (2) 14 (2019)
117. Melo A M et al. *Adv. Opt. Technol.* **2012** 530512 (2012)
118. Ma Y et al. *Opt. Lett.* **35** 469 (2010)
119. Bark H S et al. *Sci. Rep.* **11** 1307 (2021)
120. Liu D et al. *Opt. Express* **29** 24779 (2021)
121. Liu D et al. *Opt. Lett.* **46** 4370 (2021)
122. Shahounvand H, Fard A, Tavakoli M B *Opt. Quantum Electron.* **54** 120 (2022)
123. Landy N I et al. *Phys. Rev. Lett.* **100** 207402 (2008)
124. Tao H et al. *Opt. Express* **16** 7181 (2008)
125. Tao H et al. *Phys. Rev. B* **78** 241103 (2008)
126. Diem M, Koschny T, Soukoulis C M *Phys. Rev. B* **79** 033101 (2009)
127. Landy N I et al. *Phys. Rev. B* **79** 125104 (2009)
128. Shchegolkov D Yu et al. *Phys. Rev. B* **82** 205117 (2010)
129. Li Y et al. *J. Phys. D* **42** 095408 (2009)
130. Chen H-T et al. *Phys. Rev. Lett.* **105** 073901 (2010)
131. Wen Q-Y et al. *Opt. Express* **17** 20256 (2009)
132. O'Hara J, Azad A K, Taylor A J *Eur. Phys. J. D* **58** 243 (2010)

133. Richards P L *J. Appl. Phys.* **76** 1 (1994)
134. Kuznetsov S A et al. *Appl. Phys. Lett.* **99** 023501 (2011)
135. Ye Y Q, Jin Y, He S *J. Opt. Soc. Am. B* **27** 498 (2010)
136. Wen Q-Y et al. *Appl. Phys. Lett.* **95** 241111 (2009)
137. Tao H et al. *J. Phys. D* **43** 225102 (2010)
138. Engheta N, Ziolkowski R W (Eds) *Metamaterials*: *Physics and Engineering Explorations* (New York: Wiley, IEEE Press, 2006) DOI:10.1002/0471784192
139. Balanis C A *Modern Antenna Handbook* (New York: John Wiley and Sons, 2008) DOI:10.1002/9780470294154
140. Capolino F *Theory and Phenomena of Metamaterials* (Boca Raton, FL: CRC Press, 2009) DOI:10.1201/9781420054262
141. Kul'chitskii N A et al. *Usp. Prikl. Fiz.* **10** (2) 203 (2022)
142. Chen H-T et al. *Nature* **444** 597 (2006)
143. Prasankumar R P et al. *Appl. Phys. Lett.* **86** 201107 (2005)
144. Chen H-T et al. *Opt. Lett.* **32** 1620 (2007)
145. Azad A K et al. *Appl. Phys. Lett.* **95** 011105 (2009)
146. Chen H-T et al. *Nature Photon.* **2** 295 (2008)
147. Shen N-H et al. *Phys. Rev. B* **79** 161102 (2009)
148. Syzranov V S et al. *Instrum. Exp. Tech.* **55** 673 (2012); *Prib. Tekh. Eksp.* (6) 70 (2012)
149. Chen Y C et al. *Appl. Phys. Express* **5** 012201 (2012)
150. THz high-pass filters. TYDEX. Available online, https://www.tydexoptics.com/pdf/ru/High-Pass-Filters_ru.pdf
151. Edelman V S, Tarasov M A, Chekushkin A M "Capillary quasioptical highpass filter," in *Proc. of the 25th Intern. Symp. on Space Terahertz Technology, 27–30 April 2014, Moscow, Russia* Vol. 1, pp. 46–48
152. Standard filters. Multi-mesh filters. THz optical components. QMC Instruments Ltd. Available online, https://www.terahertz.co.uk/qmci/thz-optical-components/multi-mesh-filters/standard
153. Chen C-C *IEEE Trans. Microwave Theory Tech.* **21** 1 (1973)
154. Walther M et al. *Appl. Phys. Lett.* **95** 251107 (2009)
155. Takano K et al. *Appl. Phys. Express* **3** 016701 (2010)
156. Hor Y L et al. *Appl. Opt.* **49** 1179 (2010)
157. Kaur A et al., in *Proc. of the IEEE 65th Electronic Components and Technology Conf., ECTC, 26–29 May 2015, San Diego, CA, USA* (Piscataway, NJ: IEEE, 2015) pp. 2071–2076, DOI:10.1109/ECTC.2015.7159888
158. Aznabet M et al. *Opt. Express* **16** 18312 (2008)
159. Tao H et al. *J. Phys. D* **41** 232004 (2008)
160. Miyamaru F, Takeda M W, Taima K *Appl. Phys. Express* **2** 042001 (2009)
161. Liu X et al. *Appl. Phys. Lett.* **96** 011906 (2010)
162. Tao H et al. *Adv. Mater.* **22** 3527 (2010)
163. Bruning J *Proc. SPIE* **652** 6520 (2007)
164. Spiro P *Electroforming*: *A Comprehensive Survey of Theory, Practice and Commercial Applications* (Teddington: Draper, 1971)
165. Holloway C L et al. *Metamaterials* **3** 100 (2009)
166. Gokkavas M et al. *Phys. Rev. B* **73** 193103 (2006)
167. Casse B D F et al. *Appl. Phys. Lett.* **90** 254106 (2007)
168. Azad A et al. *THz Sci. Technol.* **2** 15 (2009)
169. Peralta X G et al. *Appl. Phys. Lett.* **94** 161113 (2009)
170. Miyamaru F et al. *Appl. Phys. Lett.* **96** 081105 (2010)
171. Tao H et al. *Phys. Rev. Lett.* **103** 147401 (2009)
172. Randhawa J S et al. *Appl. Phys. Lett.* **96** 191108 (2010)
173. Burckel D B et al. *Adv. Mater.* **22** 3171 (2010)
174. Wendt J R et al. *J. Vac. Sci. Technol. B* **28** C6O30 (2010) DOI:10.1116/1.3504586
175. Han M et al. *Micromachines* **13** 1170 (2022)
176. Kaveev A K, Kropotov G I *Phys. Usp.* **68** 294 (2025); *Usp. Fiz. Nauk* **195** 311 (2025)
177. Bloom A L *J. Opt. Soc. Am.* **64** 447 (1974)
178. Kobtsev S M *Opt. Spectrosc.* **63** 672 (1987); *Opt. Spektrosk.* **63** 1139 (1987)
179. Lee Y L et al. *Opt. Lett.* **32** 2813 (2007)
180. Evans J W *J. Opt. Soc. Am.* **48** 142 (1958)
181. Zhou Y et al. *J. Opt. Soc. Am. A* **20** 733 (2003)
182. Shabtay G et al. *Opt. Express* **10** 1534 (2002)
183. Yang X et al. *J. Opt. Soc. Am. A* **22** 752 (2005)
184. Wang X, Yao J *Appl. Opt.* **31** 4505 (1992)
185. Preuss D R, Gole J L *Appl. Opt.* **19** 702 (1980)
186. Mentel J, Schmidt E, Mavrudis T *Appl. Opt.* **31** 5022 (1992)
187. Title A M *Appl. Opt.* **15** 2871 (1976)
188. von Willisen F K *Appl. Opt.* **5** 97 (1966)
189. Title A M *Appl. Opt.* **14** 445 (1975)
190. Yang D et al. *Opt. Fiber Technol.* **80** 103426 (2023)
191. Melich R, Melich Z, Šolc I, in *The Physics of Chromospheric Plasmas. Proc. of the Conf., 9–13 October, 2006, Coimbra, Portugal* (ASP Conf. Ser., Vol. 368, Eds P Heinzel, I Dorotovič, R J Rutten) (San Francisco, CA: Astronomical Society of the Pacific, 2007) p. 621
192. Yu X J et al. *Displays* **3** 145 (2002)
193. Yeh P *Opt. Commun.* **29** 1 (1979)
194. Yariv A, Yeh P, in *Optical Waves in Crystal*: *Propagation and Control of Laser Radiation* (New York: John Wiley and Sons, 1984) pp. 32–158
195. Chen C-Y et al. *Appl. Phys. Lett.* **88** 101107 (2006)
196. Šolc I *J. Opt. Soc. Am.* **55** 621 (1965)
197. Pinnow D A et al. *Appl. Phys. Lett.* **34** 391 (1979)
198. Tarry H A *Electron. Lett.* **11** 471 (1975)
199. Ho I-C et al. *Opt. Lett.* **33** 1401 (2008)
200. Jones R C *J. Opt. Soc. Am.* **31** 488 (1941)
201. Vasil'ev N, Zelevinskii A "Mnogochleny Chebysheva i rekurrentnye sootnosheniya" ("Chebyshev polynomials and recurrence relations") *Kvant* (1) 12 (1982)
202. Zhou Y et al. *J. Opt. Soc. Am. A* **20** 733 (2003)
203. Melich R, Melich Z, Šolc I *Proc. SPIE* **7018** 701854 (2008)
204. Yeh P *Opt. Commun.* **29** 1 (1979)
205. Ghosh A, Chakraborty A K *Opt. Acta Int. J. Opt.* **29** 1407 (1982)
206. Kuan W-H et al., arXiv:2103.13779
207. Jung H *Int. J. Opt.* **2010** 626583 (2010) DOI:10.1155/2010/626583
208. Hong H-G et al. *Opt. Express* **17** 15455 (2009)
209. Kaveev A K et al. *Appl. Opt.* **53** 5410 (2014)
210. THz tunable polarization converter. TYDEX. Available online, https://www.tydexoptics.com/ru/products/thz_polarizers/tunable_thz_polarization_converter/
211. Gay-Balmaz P, Maccio C, Martin O J F *Appl. Phys. Lett.* **81** 2896 (2002)
212. Muravev V M et al. *Phys. Rev. Applied* **21** 034041 (2024)
213. Gallant A J et al. *J. Appl. Phys.* **102** 023102 (2007)
214. Yee K *IEEE Trans. Antennas Propag.* **14** 302 (1966) DOI:10.1109/TAP.1966.1138693
215. Gomon D A et al. *Nauchno-tekh. Vestn. Inform. Tekhnol., Mekh. Opt.* **19** 775 (2019) DOI:10.17586/2226-1494-2019-19-5-775-782
216. Odit M et al. "Tunable THz band-pass filter," in *Metamaterials 2012. The 6th Intern. Congress on Advanced Electromagnetic Materials in Microwaves and Optics, 17–22 September 2012, St. Petersburg, Russia, 2012*, pp. 541–543
217. Li C et al. *J. Electromagn. Waves Appl.* **32** 2481 (2018)
218. Azimbeik M et al. *Optik* **198** 163246 (2019)
219. Mohammadi G, Orouji A, Danaie M *Results Opt.* **13** 100575 (2023)
220. Tian Z et al. *Opt. Express* **32** 24251 (2024)
221. Stecher M et al. "Fiber Drawn 2D polymeric photonic crystal THz filters," in *Conf. on Lasers and Electro-Optics 2012, San Jose, CA, USA, 6–11 May 2012* (OSA Technical Digest) (Washington, DC: Optica Publ. Group, 2012) paper CM4J.2, DOI:10.1364/CLEO_SI.2012.CM4J.2
222. Yuan J et al. *Results Phys.* **13** 102198 (2019)
223. Lee E-S, Jeon T-I *J. Opt. Soc. Korea* **13** 423 (2009)
224. Wang J, Guo K, Guo Z *AIP Adv.* **9** 045106 (2019)
225. Withayachumnankul W, Fischer B M, Abbott D *Opt. Commun.* **281** 2374 (2008)
226. Beheshti Asl A, Rostami A, Amiri I S *Opt. Quantum Electron.* **52** 155 (2020)
227. Hussain S, Min Woo J, Jang J-H *Appl. Phys. Lett.* **101** 091103 (2012)
228. Chen Y, Cheng J, Liang C *Adv. Condens. Matter Phys.* **2020** 3902835 (2020) DOI:10.1155/2020/3902835
229. Drysdale T D, Blaikie R J, Cumming D R S *Proc. SPIE* **5070** 89 (2003)
230. Drysdale T D, Blaikie R J, Cumming D R S *Appl. Phys. Lett.* **83** 5362 (2003)
231. Gregory I S et al. *Appl. Phys. Lett.* **87** 034106 (2005)
232. Drysdale T D et al. *Microelectron. Eng.* **73–74** 441 (2004)
233. Němec H et al. *Opt. Lett.* **30** 549 (2005)
234. Li J *Opt. Commun.* **283** 2647 (2010)
235. Villa F, Gaspar-Armenta J A *Opt. Express* **12** 2338 (2004)
236. Jacob D K, Dunn S C, Moharam M G *Appl. Opt.* **41** 1241 (2002)
237. Mendis R et al. *Appl. Phys. Lett.* **97** 131106 (2010)
238. Zhao Y, Grischkowsky D *Opt. Lett.* **31** 1534 (2006)